

FY21 Progress on Computational Modeling of Water-Based NSTF

Nuclear Science and Engineering Division

About Argonne National Laboratory

Argonne is a U.S. Department of Energy laboratory managed by UChicago Argonne, LLC under contract DE-AC02-06CH11357. The Laboratory's main facility is outside Chicago, at 9700 South Cass Avenue, Argonne, Illinois 60439. For information about Argonne and its pioneering science and technology programs, see www.anl.gov.

DOCUMENT AVAILABILITY

Online Access: U.S. Department of Energy (DOE) reports produced after 1991 and a growing number of pre-1991 documents are available free via DOE's SciTech Connect (<http://www.osti.gov/scitech/>)

Reports not in digital format may be purchased by the public from the National Technical Information Service (NTIS):

U.S. Department of Commerce
National Technical Information Service
5301 Shawnee Rd
Alexandria, VA 22312
www.ntis.gov
Phone: (800) 553-NTIS (6847) or (703) 605-6000
Fax: (703) 605-6900
Email: **orders@ntis.gov**

Reports not in digital format are available to DOE and DOE contractors from the Office of Scientific and Technical Information (OSTI):

U.S. Department of Energy
Office of Scientific and Technical Information
P.O. Box 62
Oak Ridge, TN 37831-0062
www.osti.gov
Phone: (865) 576-8401
Fax: (865) 576-5728

Disclaimer

This report was prepared as an account of work sponsored by an agency of the United States Government. Neither the United States Government nor any agency thereof, nor UChicago Argonne, LLC, nor any of their employees or officers, makes any warranty, express or implied, or assumes any legal liability or responsibility for the accuracy, completeness, or usefulness of any information, apparatus, product, or process disclosed, or represents that its use would not infringe privately owned rights. Reference herein to any specific commercial product, process, or service by trade name, trademark, manufacturer, or otherwise, does not necessarily constitute or imply its endorsement, recommendation, or favoring by the United States Government or any agency thereof. The views and opinions of document authors expressed herein do not necessarily state or reflect those of the United States Government or any agency thereof, Argonne National Laboratory, or UChicago Argonne, LLC

FY21 Progress on Computational Modeling of Water-Based NSTF

prepared by
Q. Lv, A. Kraus, Z.J. Ooi, R. Hu, D. Lisowski

Nuclear Science and Engineering Division, Argonne National Laboratory

September 2021

ABSTRACT

This report documents the FY21 progress and achievements made in the computational analyses of the water-based NSTF. Both system-level and high-fidelity Computational Fluid Dynamics (CFD) analyses were performed to gain a complete understanding of the complex flow and heat transfer phenomena in natural convection systems. The progress on the water-based NSTF experimental testing is summarized in a companion report (ANL-ART-230).

As a continuation of progress from previous years, in FY21 the RELAP5 model of the NSTF was first updated to include a representative heated cavity that incorporated convection and conduction means of heat transfer. Two different cavity models were developed, one that models the radiation heat exchange among all surfaces in one enclosure (Cavity Model 1), and another that employs multiple radiation enclosures with each considering the surfaces at one axial level (Cavity Model 2). This updated RELAP5 deck was benchmarked with single-phase test data to tune form loss coefficients of the elbows and tees, along with heat transfer coefficients within the cavity and off the external insulation panels. This tuned model was then found to accurately predict fluid temperatures within 2.5% and both system and riser flow rates within 6% during single-phase, steady-state simulations. For transient simulations, there is a slight over prediction of the flow rate, fluid temperatures, and heater temperatures during the heat-up period, which indicate that the transient heat loss may be underestimated.

Following, the capabilities of RELAP5-3D were examined, which feature a conduction enclosure model that is not present in the current version of RELAP5-MOD3.3 used for all previous NSTF simulations. As an initial comparison of the two codes, single-phase simulations were run that used similar input decks. The results indicate that the single-phase flow predicted by the two codes was very similar, however RELAP5-3D appears to predict a higher system flow during the two-phase transient when compared to the flow rates predicted by RELAP5-MOD3.3. Furthermore, RELAP5-3D run did not capture the density wave oscillations or geysering phenomena, which are large oscillation flow instabilities observed in the experimental facility. To further the prediction capabilities for capturing two-phase instabilities, Options 55, 57, 58, 61, which are implemented by default in RELAP5-MOD3.3 but not in RELAP5-3D, were investigated. When enabling Option 61, RELAP5-3D agrees well with MOD3.3 in predicting the total system flow, while other options have negligible effect on the predicted total system flow by RELAP5-3D. However, none of these options enables RELAP5-3D to produce the same flow instabilities. For future steps, efforts are currently underway to investigate RELAP5-3D's different behavior in predicting low-pressure two-phase instabilities.

STAR-CCM+ was used to perform CFD analysis of the water-based test facility and provide simulation results for comparisons to experimental data. Efforts first focused on describing the characteristics of flow within the heated cavity. A study was performed on whether possible leakage flow between the two sides of the cavity could substantially impact and explain the results. An additional second assumption was examined which defined adiabatic side walls, so physical insulation structures were added to the models to allow conduction across this outer insulation. The results suggest that potential porosity of the insulation could be a major factor in the temperature distribution within the cavity and should be considered in any studies where it is desirable to know the cavity wall temperatures to higher accuracy.

Following, CFD simulations were performed which modeled the inlet and outlet headers in detail to establish any potential nonuniformity of the flow caused by the headers, and its impact on temperatures and flow behavior in the cavity region. Corroborating experimental observations, results from the CFD module yield reduced mass flow in Riser 1 and elevated mass flow in Riser 8. These features combine to create an asymmetric temperature profile across the risers. The explicit modeling of the flow in the headers and cavity provides evidence that the system and instruments are functioning correctly and that the skewed temperature distribution is indeed physical.

Finally, steps were taken toward expansion of the modeling practices by the design and initialization of an LES unit cell computation, and design and testing of a full-geometry CFD model of the as-built NSTF. The LES model will provide beneficial reference data in the lack of experimental velocity data in the heated cavity, while the full simulation will support detailed standalone CFD simulation and facilitate coupled RELAP5/CFD simulations of transients in the future.

Table of Contents

ABSTRACT.....	i
Table of Contents	iii
List of Figures	iv
List of Tables	vi
1 Introduction.....	1
2 System Level Modeling of Water-Based NSTF	4
2.1 Model Description	4
2.2 Cavity Modeling Study	6
2.2.1 Cavity Model 1	7
2.2.2 Cavity Model 2	14
2.3 Code Benchmark using Single-phase Test Data	17
2.4 Code Benchmark using Transient Test Data	26
2.5 Code comparison between RELAP5-3D and RELAP5-MOD3.3	28
2.6 Summary and Future Work.....	30
3 CFD Analyses of Water-Cooled NSTF	33
3.1 CFD Model Description.....	33
3.2 Stand-alone Cavity Modeling	34
3.2.1 Insulation Porosity	37
3.2.2 External Insulation Heat Transfer	40
3.2.3 Impacts of Header Geometry	44
3.3 Large Eddy Simulation of a Cavity Unit Cell.....	48
3.4 Single-phase Full System Simulation	51
3.5 Summary and Future Work.....	53
References	55
Acknowledgements	55

LIST OF FIGURES

Figure 1-1: Solid model rendering of water NSTF facility.....	3
Figure 2-1. Nodalization diagram of the RELAP5 model for the water-based NSTF.....	5
Figure 2-2: Model for the water tank and the active cooling in the NSTF.....	6
Figure 2-3. Top view of the modeled cavity.....	7
Figure 2-4. Predicted total system flow by cavity model 1.	8
Figure 2-5. Outer surface temperatures at riser tube bottom.	9
Figure 2-6. Outer surface temperatures at riser tube center.	9
Figure 2-7. Outer surface temperatures at riser tube top.	10
Figure 2-8. Riser tube 1 outer surface temperature axial distribution.	10
Figure 2-9. Riser outer surface temperature comparison between cases with and without cavity at Riser 4 center.	11
Figure 2-10. Heat flux distribution across the riser tubes at the bottom.....	11
Figure 2-11. Heat flux distribution across the riser tubes at the center.	12
Figure 2-12. Heat flux distribution across the riser tubes at the top.	12
Figure 2-13. Heat flux distribution along riser tube 1.	13
Figure 2-14. Heated plate surface temperature axial distribution.....	13
Figure 2-15. Heated plate surface temperature axial distribution (zoom-in).....	14
Figure 2-16. Comparison of predicted total system flow between the two cavity models.	15
Figure 2-17. Comparison of heated plate inner surface temperature at the center	16
Figure 2-18. Comparison of riser tube outer surface temperature at center of riser tube 4	16
Figure 2-19. Heated plate inner surface temperatures with cavity model 2	17
Figure 2-20. Benchmark results for the loop behaviors, fluid temperatures.	20
Figure 2-21. Benchmark results for the loop behaviors, flow rates.....	21
Figure 2-23. Comparison of the predicted average heated plate temperatures with respect to fouling factors of only the riser surface natural convection heat transfer coefficient.	24
Figure 2-24. Comparison of the predicted average heated plate temperatures with respect to fouling factors of both the riser surface and the heated plate surface natural convection heat transfer coefficient.	24
Figure 2-25. Comparison of the predicted average heater temperatures with respect to the heater surface emissivity.....	25
Figure 2-26. Comparison of the predicted cavity exterior temperatures with respect to the enhancement factors of the heat loss heat transfer coefficient.	25
Figure 2-27. Comparison of the predicted average heater temperatures with respect to the reduction factors of the heater thermal conductivity.	26
Figure 2-28. System flow rate.....	27
Figure 2-29. Test section inlet/outlet temperatures.....	27
Figure 2-30. Heater temperatures.	28
Figure 2-31. Leak air flow from RELAP5 model.....	28
Figure 2-32. Comparison between RELAP5-3D and MOD 3.3 in predicting the total system flow for the two-phase baseline case.....	30
Figure 3-1. CAD geometry of the primary water-cooled NSTF flow path, including the heated cavity.....	34
Figure 3-2. Temperature distribution at the midplane of the heated cavity for the initial simulation.....	36

Figure 3-3. Cold wall temperatures for the initial simulations.	36
Figure 3-4. Cold wall temperature distribution for the 10,000 resistance case.	38
Figure 3-5. Cold wall temperature distribution for the 100,000 resistance case.	39
Figure 3-6. Temperature distribution at the cavity midplane for the 100,000 resistance case.	40
Figure 3-7. Predicted temperature distribution for the case with external insulation modeled. Note that the white region represents a clipping of temperatures above the 450 °C axis limit.	41
Figure 3-8. Cold wall temperature distribution for the case with external insulation.	42
Figure 3-9. Riser liquid temperatures for the base case.	43
Figure 3-10. Riser liquid temperatures for the case with external insulation.	44
Figure 3-11. Expanded cavity simulation domain including the inlet and outlet headers.	45
Figure 3-12. Axial velocity at the inlet header midplane.	46
Figure 3-13. Flow streamlines at the inlet header.	46
Figure 3-14. Axial velocity at the outlet header midplane.	47
Figure 3-15. Flow streamlines at the outlet header.	47
Figure 3-16. Riser liquid temperatures for the case with headers modeled.	48
Figure 3-17. Base case axial velocity for the water-cooled NSTF cavity unit cell.	49
Figure 3-18. Axial view of the URANS unsteady axial velocity for the unit cell study.	50
Figure 3-19. Ratio of mesh size to Taylor length scale predicted by URANS.	51
Figure 3-20. Axial velocity patterns in the vicinity of the water storage tank for the full geometry model.	52
Figure 3-21. Velocity vectors for the full geometry simulation.	53

LIST OF TABLES

Table 2-1. Benchmarked form loss coefficient.	18
Table 2-2. Benchmarked NSTF loop results for single-phase test Run052.	18
Table 2-3. Benchmarked NSTF loop results for single-phase test Run051.	19
Table 2-4. Benchmarked NSTF loop results for single-phase test Run054.	19
Table 2-5. Benchmarked NSTF loop results for single-phase test Run055.	20
Table 2-6. Benchmarked steady-state cavity temperatures with a riser and heated plated heat transfer fouling factor of 1.24, a heater surface emissivity of 0.317, and a cavity exterior heat loss coefficient enhancement factor of 1.084.	23
Table 2-7. RELAP5 3D options descriptions.	29

1 Introduction

The Natural convection Shutdown heat removal Test Facility (NSTF) at Argonne National Laboratory (Argonne) was built to study the performance of passive systems for advanced nuclear reactors. It is a large-scale thermal hydraulics test facility designed to carry out highly instrumented experiments to validate the performance of Reactor Cavity Cooling System (RCCS) concepts for reactor decay heat removal that rely on natural convection cooling with either air- or water-based systems. With successful conclusion of this air-based testing program in 2016, the facility has transitioned to a water-based cooling concept with the experimental design based on a the RCCS concept designed by Framatome. The overall assembly of the water NSTF will reflect a half vertical scale and 12.5° sector slice of the full-scale concept of Framatome SC-HTGR design.

Throughout the course of computational modeling and code benchmarks of air-based NSTF tests, it was demonstrated that the computational effort significantly strengthened the experimental program. This mutually beneficial relationship between the analysis and experimental efforts has become integral to the overall program objective of examining the heat removal performance of the RCCS concept, and continued in the water-based NSTF study. The primary objective of the NSTF analyses is to assess the limitations in typical approaches for modeling this type of natural circulation RCCS concepts and validate the analysis methods and computer codes which may be used in licensing. Additionally, the NSTF analyses aid in the RCCS design optimization, and supporting experiment activities, i.e., helping assure that the experimental procedures, setup, and measurements follow best practices and produce high quality, traceable data.

This report documents the recent progress and achievements made in the computational analyses of the water-based NSTF. Both system-level and high-fidelity Computational Fluid Dynamics (CFD) analyses were performed to gain a complete understanding of the complex flow and heat transfer phenomena in natural connection systems. The primary focus of the system-level modeling was to analyze the integral system performance of the facility using RELAP5. As the NSTF is converted from air-based to water-based, more complex system behaviors are expected and observed due to two-phase flow and heat transfer. The results of the analyses help to assess the capabilities of existing mature codes, such as RELAP5, when they are used to simulate natural circulation systems involving single-phase water flow and transition to two-phase flow with atmospheric boiling. The primary focus of the CFD work is to gain further physical insight into the areas with complex three-dimensional flow, which cannot be easily done with system-level analyses. This includes areas such as the heated cavity. The quantitative CFD results can be used to amend and improve local aspects of the RELAP5 modeling, and thus potentially increase the accuracy of transient analyses.

The current system-level work is a continuation of the progress made in previous years where the system analysis efforts were focused on developing a reference model for the water-based NSTF design, verifying the scaling laws, performing pre-test simulations, and performing parametric sensitivity studies [1-1]. Detailed description of the reference model can be found in [1-1] while the physical layout of the water-based NSTF as well as the detailed dimensions can be found in [1-2]. All the piping/tank walls were modeled as heat structures, with convective

boundary condition for the inner surface and adiabatic boundary condition for the outer surface. The RELAP5 model developed in the previous study did not include the cavity. Instead, a heat flux boundary was directly applied to the outer surface of the riser tube assembly, which did not represent the real system. Utilizing the reference RELAP5 model, a parametric study of the effects of varying operational conditions and system configurations on the overall system performance was performed. The results of the parametric study provided insights into the system behaviors and guidance on system operations before conducting any experiments. Additionally, a check of the scaling law was performed on the water-based NSTF to examine any scaling distortions.

A solid model rendering of the NSTF facility is shown in Figure 1-1. A heat flux is applied to one cavity wall by an array of electric radiant heaters, which leads to the development of a natural convection loop to cool the system. In a standard test, cold water is drawn from the water tank into the “downcomer” pipe and inlet header. Flow is then split between eight riser ducts for the length of the heated cavity. These ducts all converge at an outlet header, where flow mixes and then enters the water tank through the piping system.

The rest of this report is organized as follows. Section 2 gives detailed descriptions and results of the updated system level model of NSTF using RELAP5. Code simulations results are compared against experimental data. Section 3 focuses on the CFD analyses of the water-cooled NSTF, covering stand-alone cavity modeling, large eddy simulation of a cavity unit cell model, and full system simulation of single-phase operation. The summary and future work of the system level and CFD analyses are also presented at the end of each respective Section.

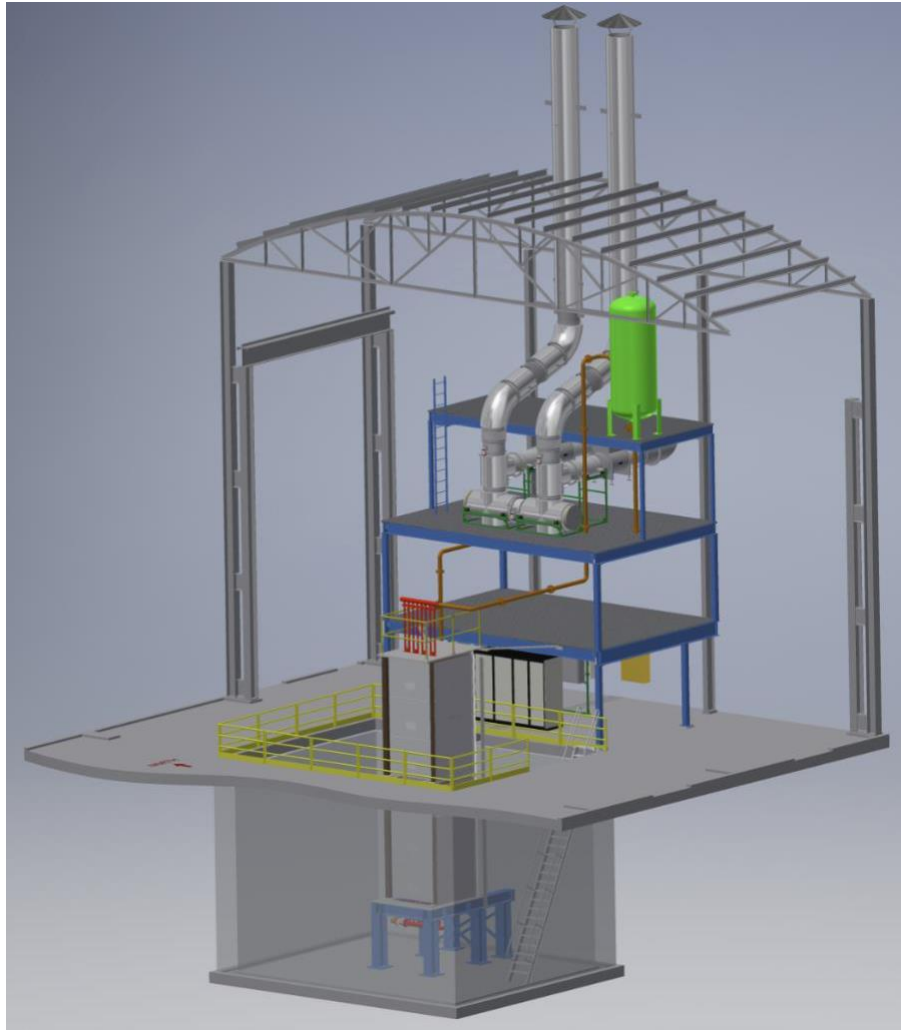


Figure 1-1: Solid model rendering of water NSTF facility

References

- [1-1] Lv, Q., Kraus, A., Hu, R., Bucknor, M., Lisowski, D., & Nunez, D. (2017). Progress Report on Computational Analyses of Water-Based NSTF. ANL-ART-103, Argonne National Laboratory.
- [1-2] D. Lisowski, C. Gerardi, R. Hu, et al., “Water NSTF Design, Instrumentation, and Test Planning,” ANL-ART-98, August 2017.

2 System Level Modeling of Water-Based NSTF

2.1 Model Description

The reference RELAP5 model developed for the water-based NSTF is shown in Figure 2-1. The water tank is modeled as four volumes, namely, P980, P971, B969, and P950, which represent the air/steam region, non-thermal-mixing water region, thermal-mixing water region, and bottom half of the water tank, respectively. Following the water tank are a series of connecting pipes, including P890 – P840. The inlet and outlet headers of the riser tube assembly in the water-based NSTF are fabricated from a set of tees, which are modeled as branches in the present model, namely, B790 – B720 and B590 – B520. A total of eight risers are modeled, each consisting of an upstream non-heated region (P691 – P698), a heated region (P671 – P678), and a downstream non-heated region (P651 – P658). The riser tube assembly is connected back to the water tank through pipes of P490 – P450. All the piping is made from 4.0” Sch 40 pipes, with an ID of 4.067”. All the piping/tank walls are modeled as heat structures, with convective boundary condition for the inner surface. To model the heat loss, 2-inch-thick K-FLEX thermal insulation is modeled as part of the heat structures, and a natural convective heat loss boundary condition is applied to the outer surface.

The model of the tank, as shown in Figure 2-1, was found to be important in determining the system transient behaviors, especially the initiation of flashing, and the time for decrease of system flow. The tank modeling was mainly focused on two aspects, namely, thermal mixing inside the tank, and tank inlet nozzle connection [2-1]. In the present model, details of the active cooling loop for the NSTF single-phase operation are not modeled. Instead, two time-dependent junctions and two time-dependent volumes are employed to model the active cooling, as shown in Figure 2-1. Junction 439 and volume 998 simulate the hot water drawn into the cooling loop while junction 429 and volume 997 simulate the cooled water returning to the water tank. In the NSTF single-phase experiments, the set point of the chiller that provided the cooling was controlled to achieve a liquid riser header inlet temperature of approximately 30°C. The time dependent volume 997 models this control by providing varying boundary conditions. With this reference RELAP5 model, parametric studies of the proposed matrix testing cases were performed, and the complete details can be found in the previous report [2-1].

In the previous work, the RELAP5 model of the NSTF did not include the cavity. Instead, a heat flux boundary was directly applied to the outer surface of the riser tube assembly. Due to the thermal inertia of the cavity, as well as the thermal resistance due to the thermal radiation process, the actual transient development in the water based NSTF will be slower than predicted by the previous reference model. This motivated the effort to incorporate the cavity into the existing reference model in FY21. The modeling of the cavity is discussed in detail in a subsequent section of this chapter.

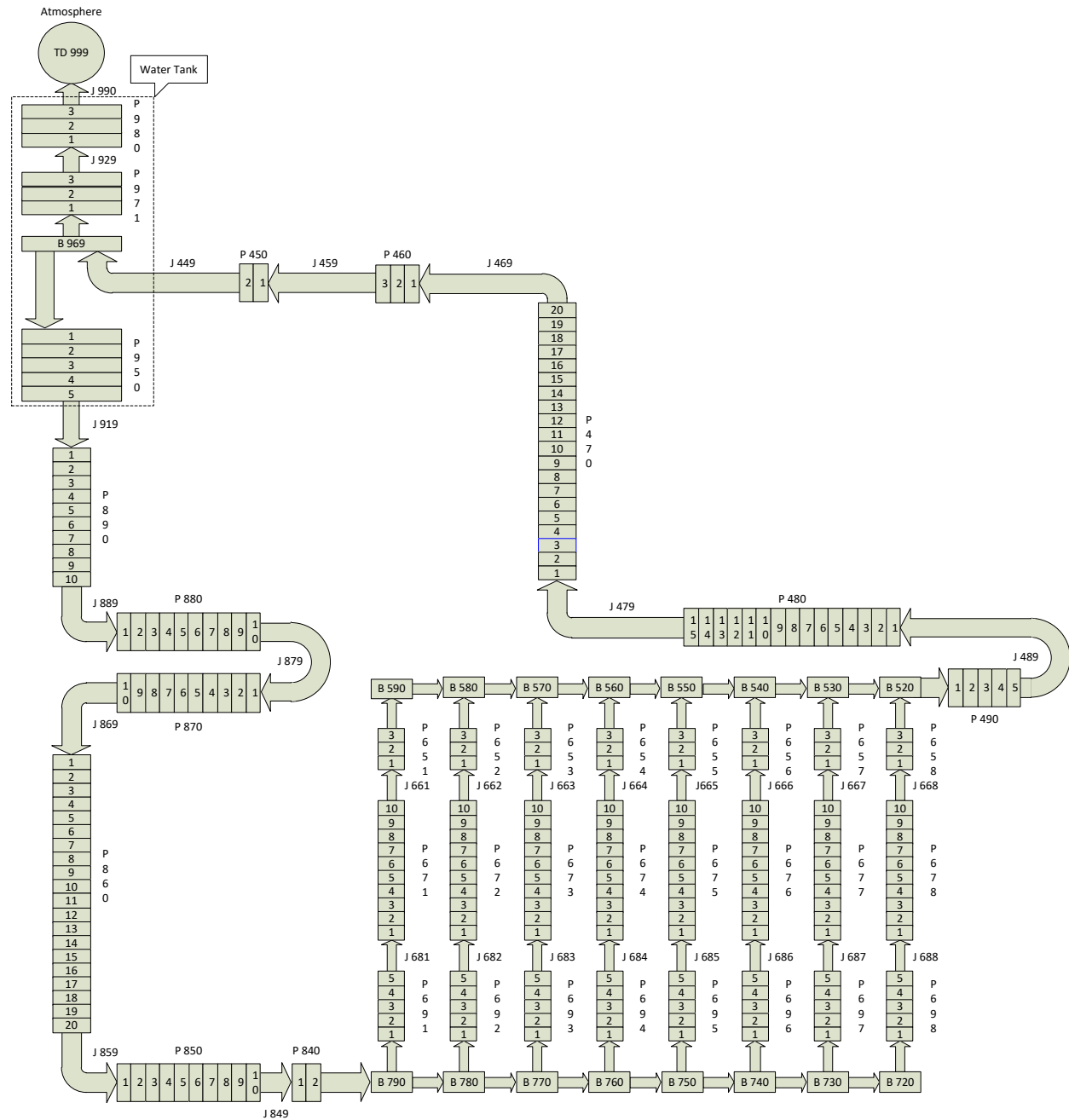


Figure 2-1. Nodalization diagram of the RELAP5 model for the water-based NSTF.

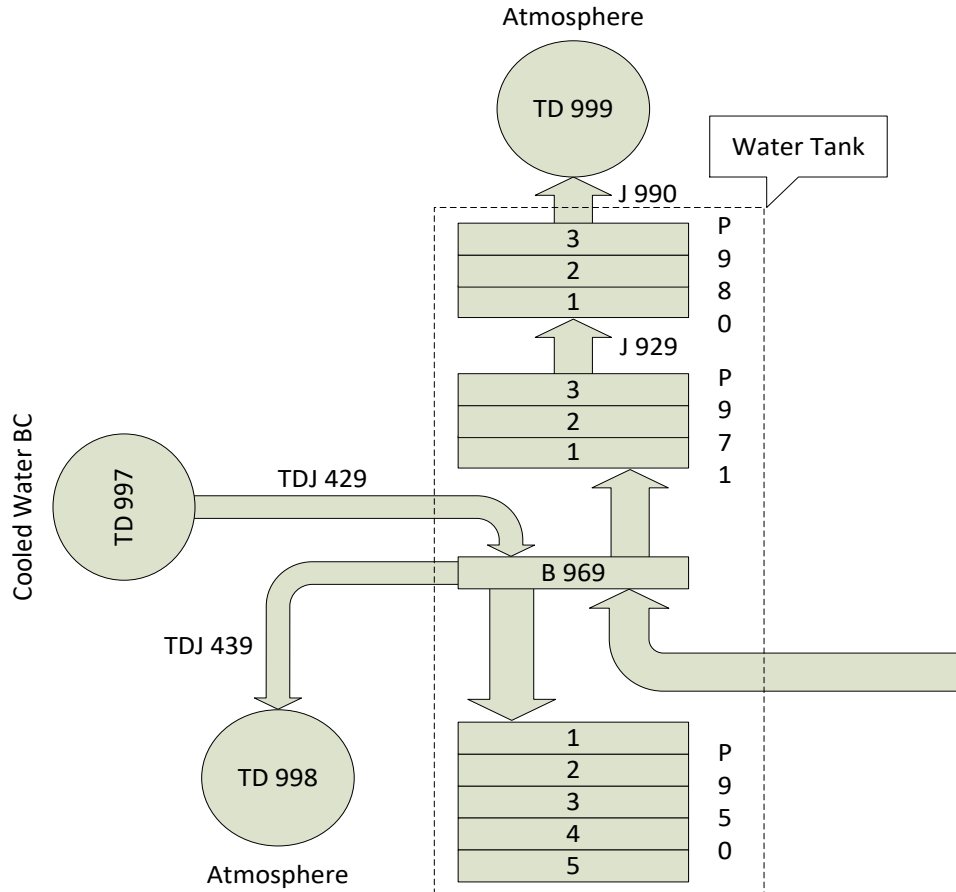


Figure 2-2: Model for the water tank and the active cooling in the NSTF.

2.2 Cavity Modeling Study

In FY21, the cavity was added to the previous RELAP5 model. The top view of the modeled cavity is shown in Figure 2-3, which consists of the eight riser tubes (including the fins), the two side walls, the heated plate, the top and bottom walls, and the insulation plates sealing the edges of the riser tube assembly. Except for the top and bottom walls, all the other surfaces are divided into eight meshes axially. Each of the top and bottom walls is considered as one mesh. A total of 98 surfaces are resulted. It should be noted that RELAP5 has a limit of 100 surfaces for its radiation enclosure, which has been accounted for during the meshing process.

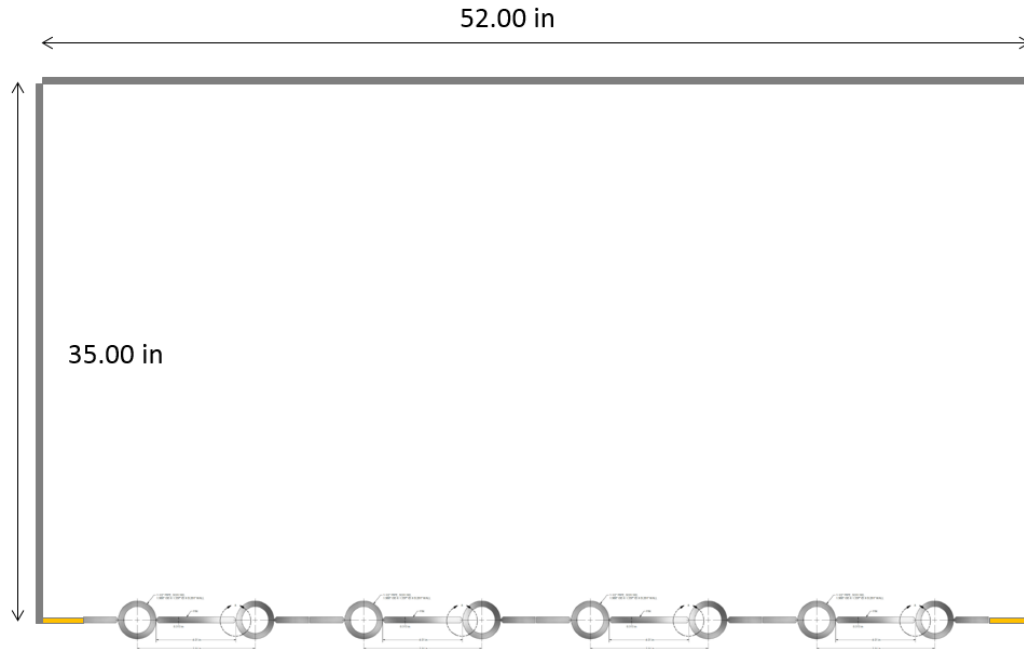


Figure 2-3. Top view of the modeled cavity.

The cavity modeling study started with investigation of two different modeling strategies. The first strategy models the radiation heat exchange among all the 98 surfaces in one enclosure. The second strategy employs multiple (8) radiation enclosures, each considering the surfaces at the same axial level. The top and bottom walls are included in the topmost and bottommost radiation enclosures, respectively. The main purpose of developing the second model is to circumvent the constraint on the number of surfaces allowed for one radiation enclosure, which will allow for finer meshing as well as radial meshing in the heated plate and side walls if needed. Both of the cavity models require input of the view factors between the surfaces, which were calculated through CFD simulations. For this modeling study, there were two simplifications made. First, the internal natural convection/circulation inside the cavity was neglected. Second, the exterior thermal insulations and heat losses were not modeled. Instead, a uniform heat flux boundary was applied directly to the back surface of the heated plate.

2.2.1 Cavity Model 1

In this section, cavity model 1 is first used to simulate the two-phase baseline case. Shown in Figure 2-4 is the predicted total system flow in comparison with that predicted by the previous reference model without cavity. The predicted total system flows from both models are alike where similar features are observed in both flows. As can be seen, with the cavity modeled, a slower transient is predicted mainly due to the increased thermal inertia from the cavity and also the additional thermal resistance corresponding to the thermal radiation process. However, the two-phase quasi-steady-state flow predicted with cavity model 1 is similar to that by the previous reference model. This is mainly because at the quasi-steady state, the cavity stops absorbing heat and thus no longer affects the system transient behavior.

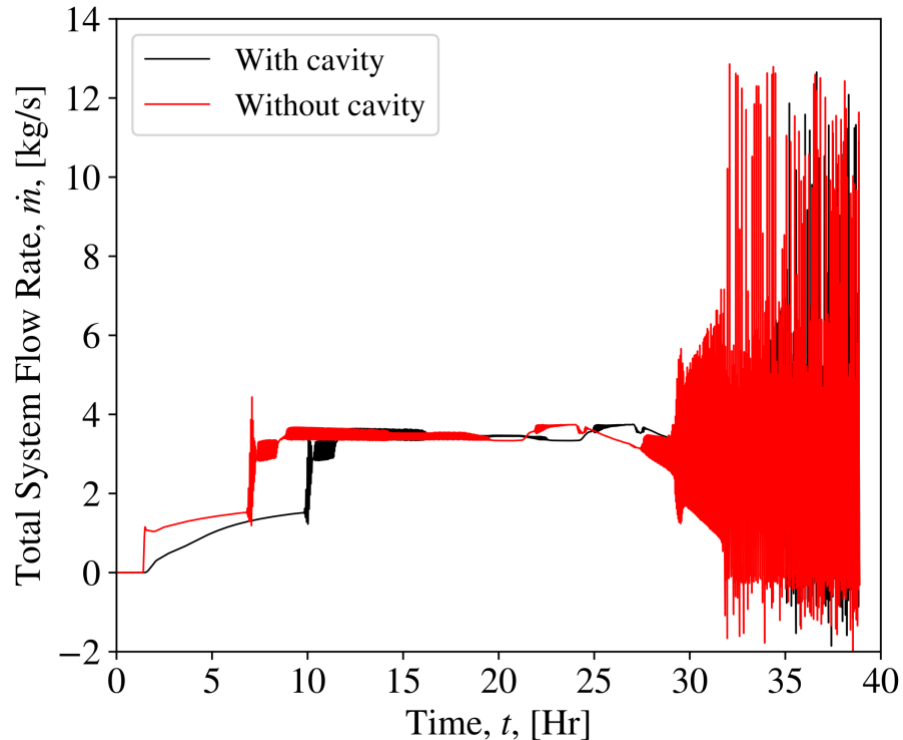


Figure 2-4. Predicted total system flow by cavity model 1.

The riser tube outer surface temperatures are shown in Figure 2-5 to Figure 2-7 where the surface temperatures for all risers are almost identical. In the initial phase, the riser temperatures increase slightly parabolically and then almost linearly until flashing initiation, after which the temperatures remain relatively constant at the quasi-steady state. As can be seen, the riser tube outer surface temperatures after flashing starts are not far above the water saturation temperatures. This is mainly due to the small thermal resistance of the tube wall and also the fact that the system water is saturated (or nearly saturated depending on the elevation) after flashing initiates. In addition, as shown in Figure 2-8, the axial temperature gradient along the riser tube outer surface seems insignificant. Figure 2-9 compares the riser tube outer surface temperature with and without the cavity. The effect of the cavity on the riser tube outer surface temperature is shown to be negligible during the quasi-steady state as the cavity stops absorbing heat and thus no longer affects the system behavior.

Shown in Figure 2-10 to Figure 2-13 are the heat flux distribution on the inner surfaces of the riser tubes over the entire assembly. As can be seen, the heat flux is fairly uniform. This is partially because a uniform heat flux was applied on the outer surface of the heated plate for this simulation. It also indicates that the radiation heat transfer between the heated plate and riser tube assembly surfaces is fairly uniform. All of that resulted in a fairly uniform temperature distribution on the inner surface of the heated plate, as shown in Figure 2-14 and Figure 2-15, where the temperature variation is within 5°C.

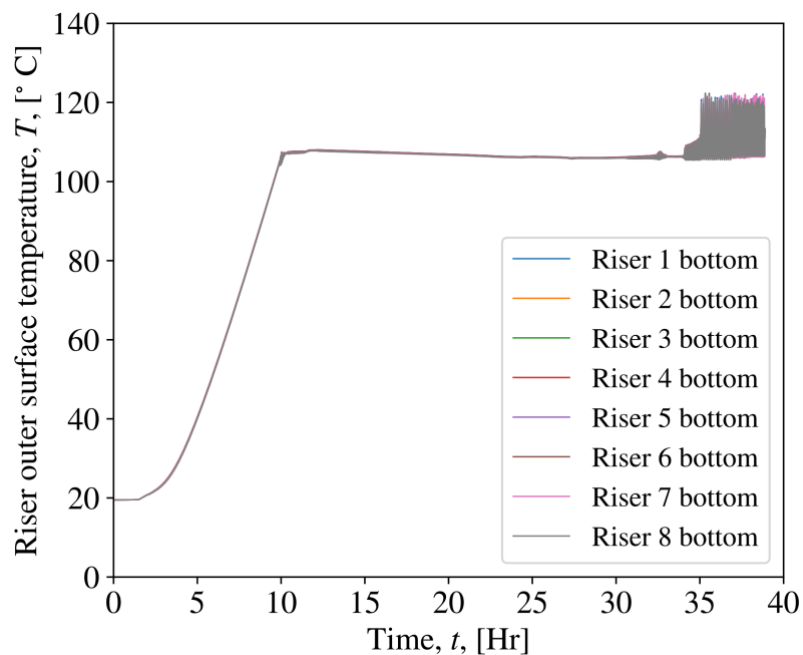


Figure 2-5. Outer surface temperatures at riser tube bottom.

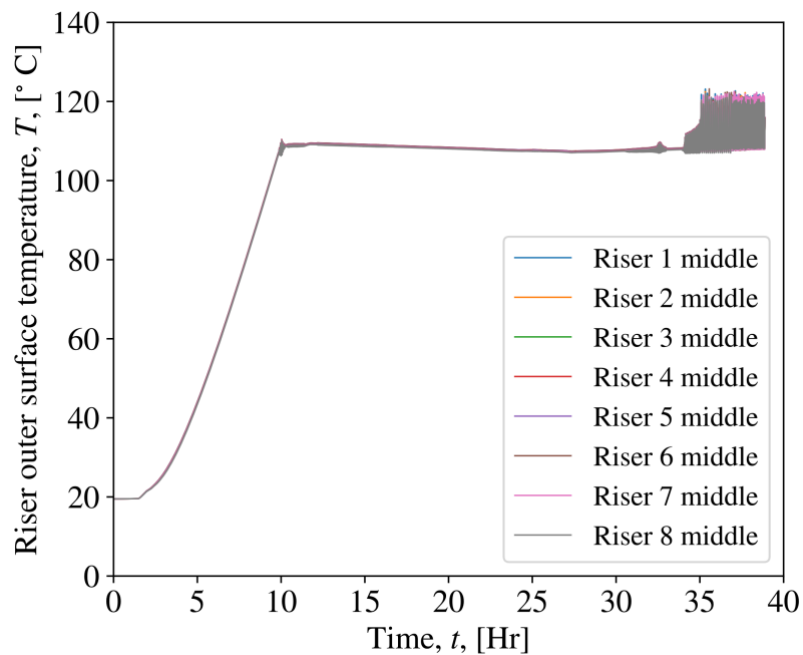


Figure 2-6. Outer surface temperatures at riser tube center.

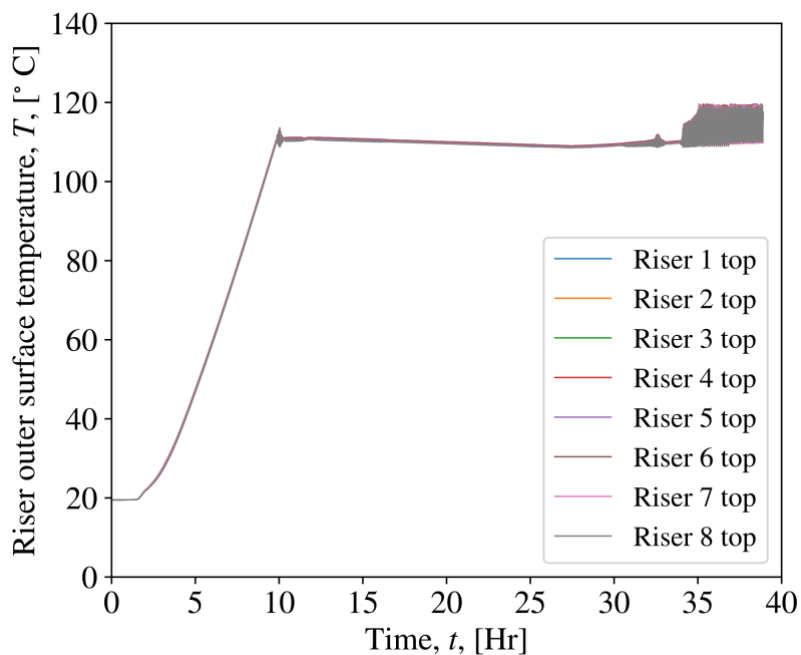


Figure 2-7. Outer surface temperatures at riser tube top.

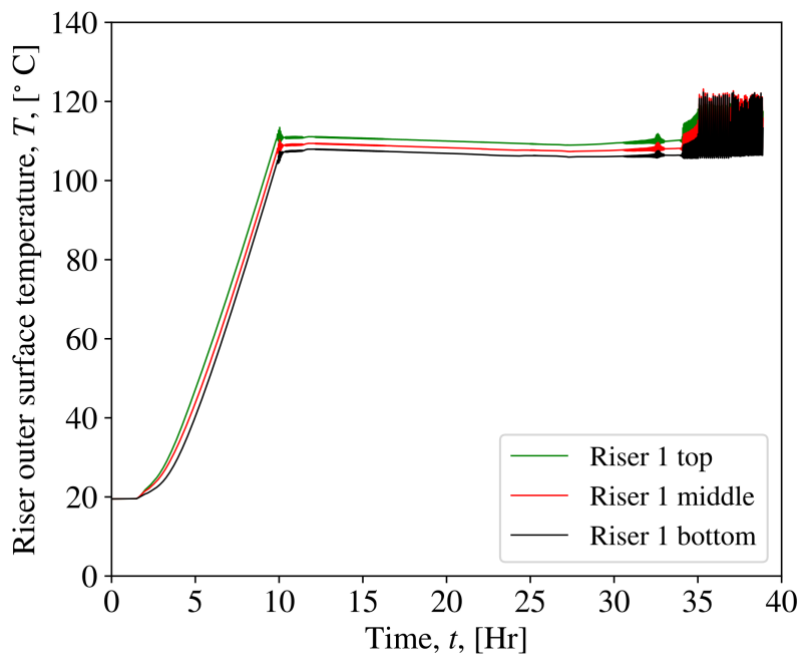


Figure 2-8. Riser tube 1 outer surface temperature axial distribution.

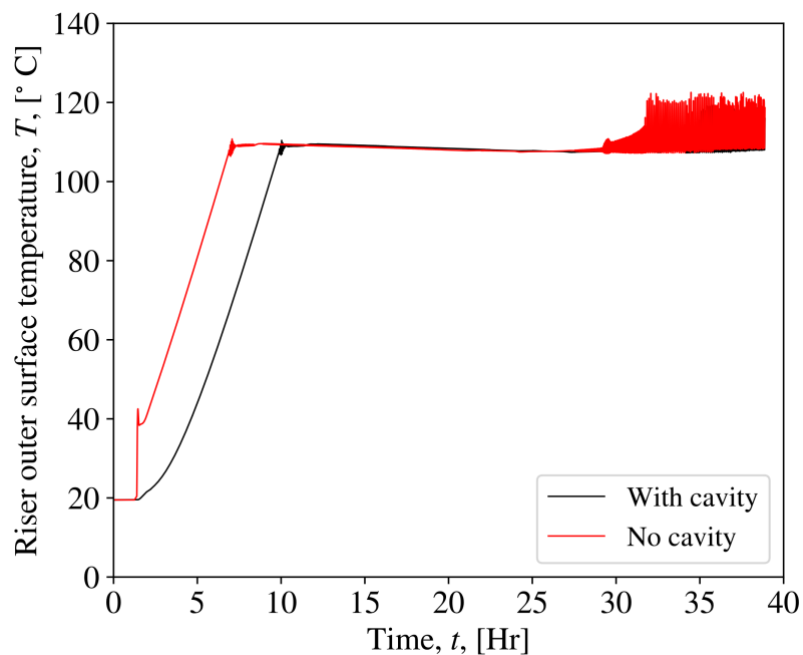


Figure 2-9. Riser outer surface temperature comparison between cases with and without cavity at Riser 4 center.

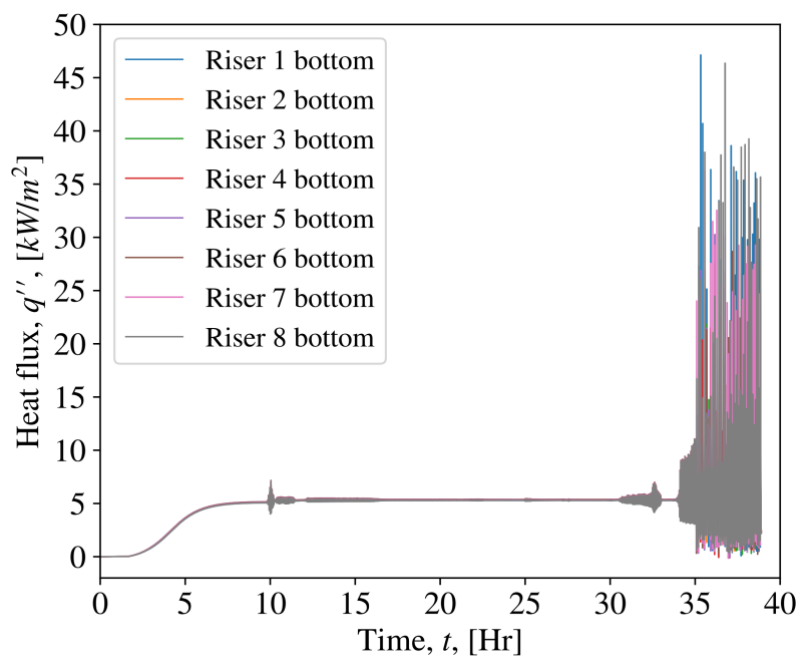


Figure 2-10. Heat flux distribution across the riser tubes at the bottom.

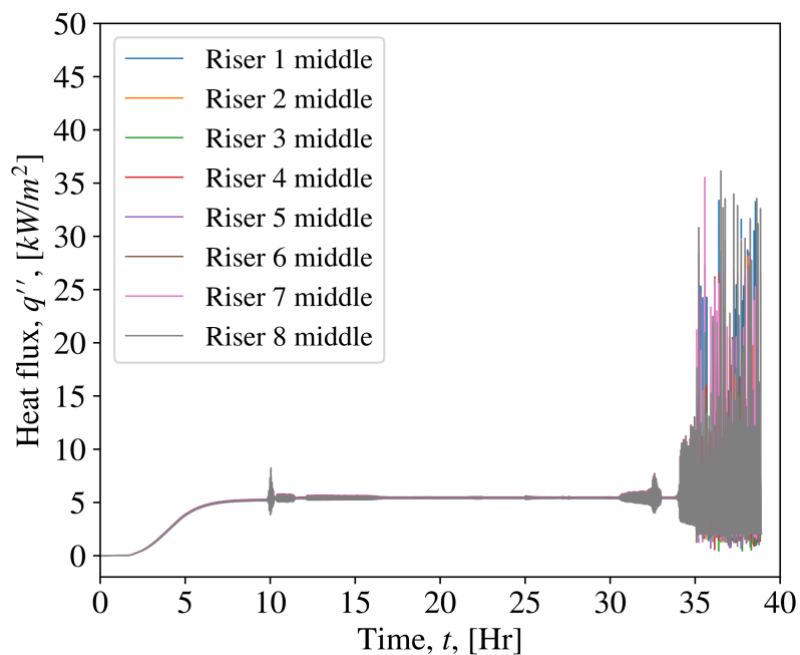


Figure 2-11. Heat flux distribution across the riser tubes at the center.

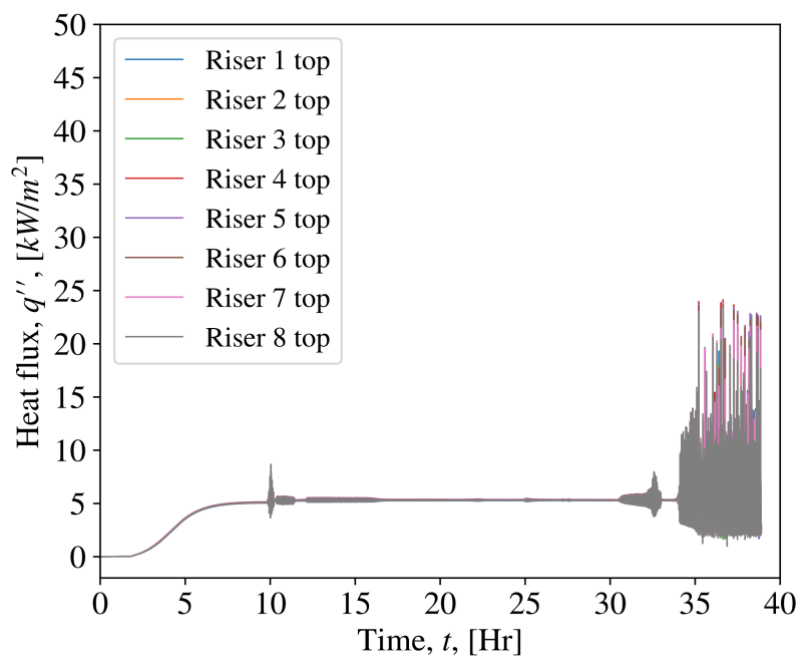


Figure 2-12. Heat flux distribution across the riser tubes at the top.

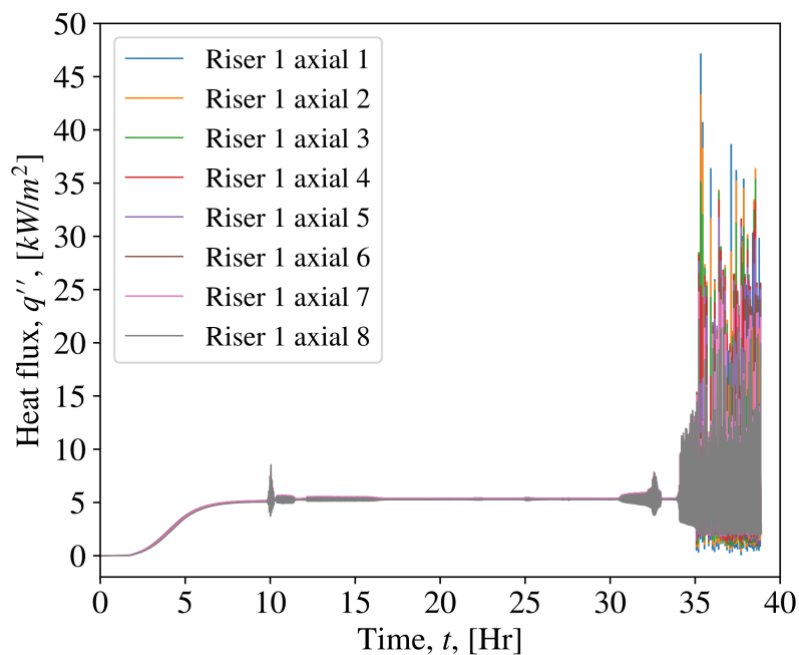


Figure 2-13. Heat flux distribution along riser tube 1.

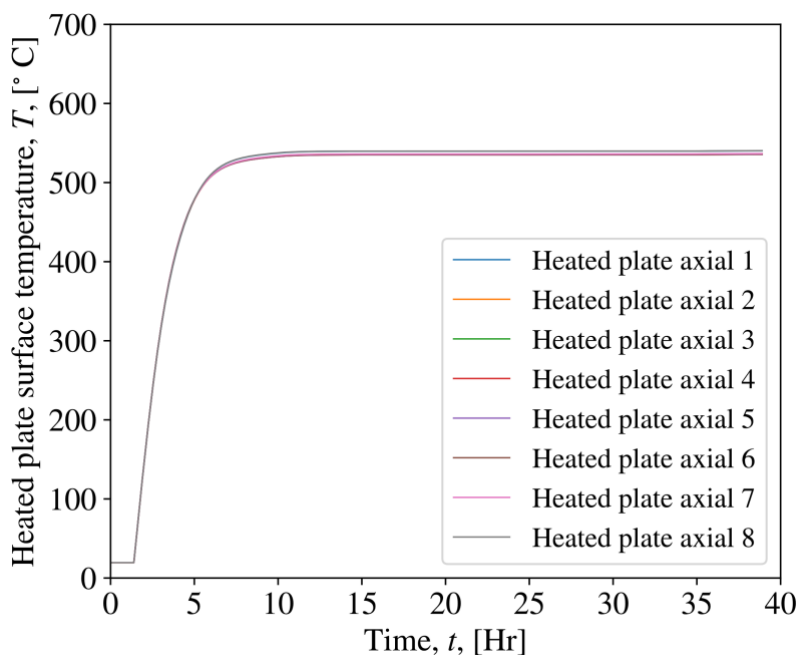


Figure 2-14. Heated plate surface temperature axial distribution.

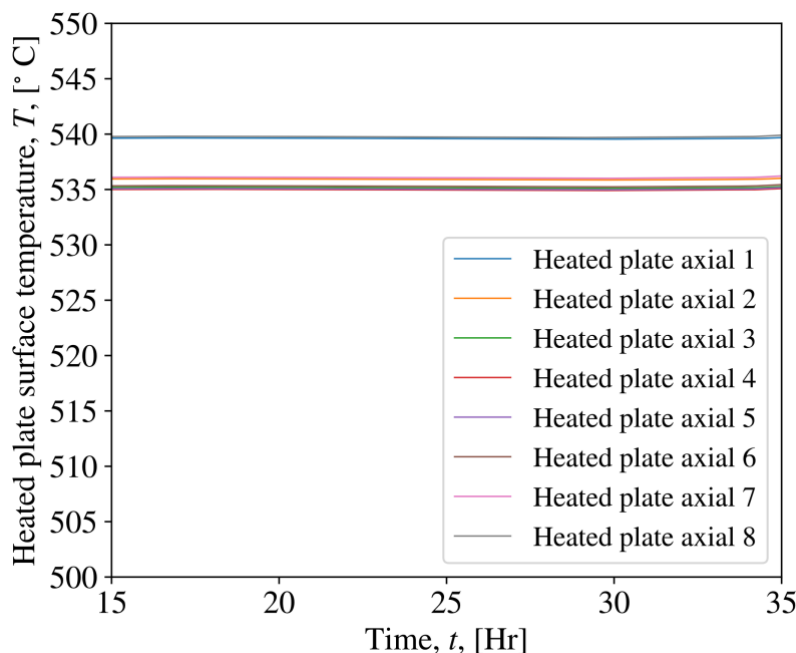


Figure 2-15. Heated plate surface temperature axial distribution (zoom-in).

2.2.2 Cavity Model 2

Since cavity model 2 employs multiple (8) radiation enclosures for each of the axial elevations, the calculation of view factors for cavity model 2 is not as straightforward as for cavity model 1. This is because there are no top and bottom surfaces for any internal enclosure, while for the top and bottom enclosure, one surface is missing. To circumvent this issue, the following method was adopted. First, a “complete” enclosure with imaginary top and bottom surfaces was assumed and the corresponding view factors were calculated. An adjustment was then made when adapting the view factors for the “complete” enclosure to the 8 actual enclosures. For any interaction between a real surface and an imaginary surface, the corresponding view factor would be merged into the self-view factor of the real surface.

The two-phase baseline case was then simulated with cavity model 2. Figure 2-16 shows the predicted total system flow comparing with that predicted by cavity model 1. The overall transient behaviors of the system flow by the two models are similar, with model 2 showing a slight delay of approximately 1300 s. With the view factor adjustment described previously, the view factors between the heated plate and riser tube assembly were reduced, indicating more resistance to the radiation heat exchange between the two surfaces. The increased thermal resistance caused the delay in the transient development for cavity model 2. Because of the same reason, cavity model 2 predicted a higher heated plate inner surface temperature than cavity model 1, as shown in Figure 2-17. However, the predicted riser tube outer surface temperatures by the two cavity models are similar, as demonstrated in Figure 2-18. This is because, as discussed earlier, the riser tube outer surface temperature is more dependent on the tube wall thermal resistance and the water temperature, which are similar in the two simulated cases.

It was also found that the predicted heated plate inner surface temperatures by cavity model 2 are not as uniform as that by cavity model 1. Instead, the predicted heated plate inner surface

temperatures are divided into two groups, as shown in Figure 2-19, one representing the internal enclosures, while the other one representing the top and bottom enclosures. The predicted heated inner surface temperatures at the internal enclosures are higher than the predicted temperatures at the top and bottom enclosures. Based on the way the view factors are adjusted, it is obvious that the internal enclosures have similar view factors while the top and bottom have similar view factors, which explains the grouping of the predicted heated plate inner surface temperatures. Furthermore, the increase of thermal radiation resistance due to the view factor adjustment is larger for the internal enclosures due to an additional missing surface. This is why the internal surfaces on the heated plate experience higher temperatures than the edge surfaces, as shown in Figure 2-19. Given that the single-enclosure model, without the additional thermal resistance, is more physical than the multiple-enclosures model, it is used for modeling the cavity for the remainder of this work.

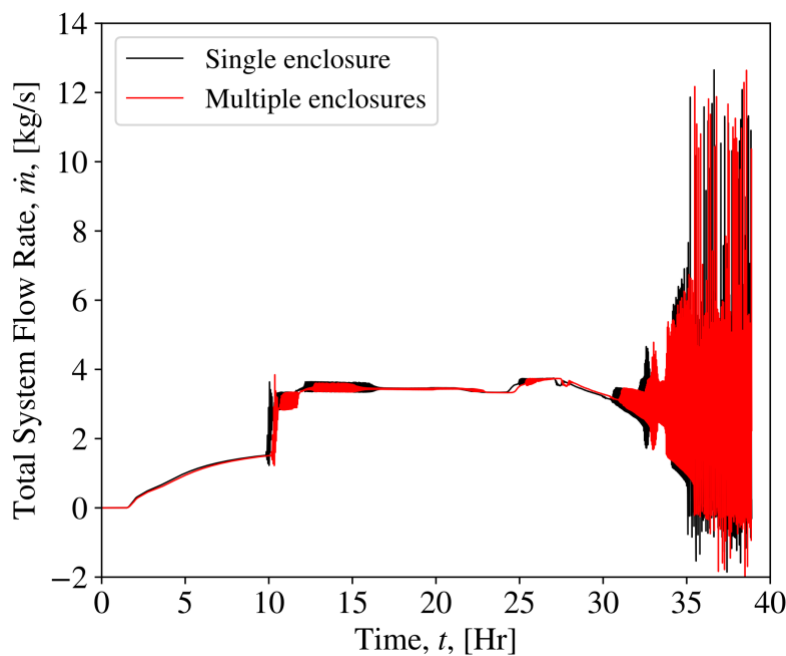


Figure 2-16. Comparison of predicted total system flow between the two cavity models.

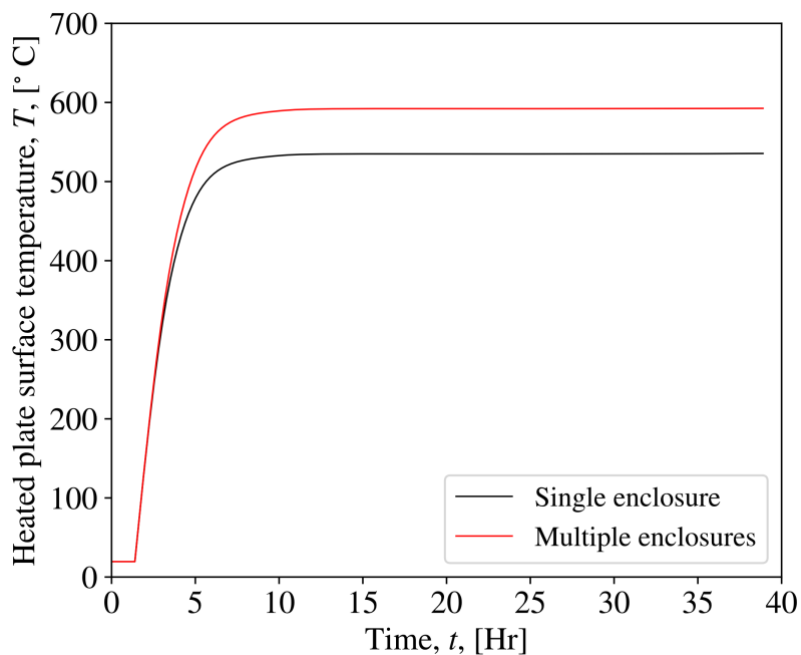


Figure 2-17. Comparison of heated plate inner surface temperature at the center

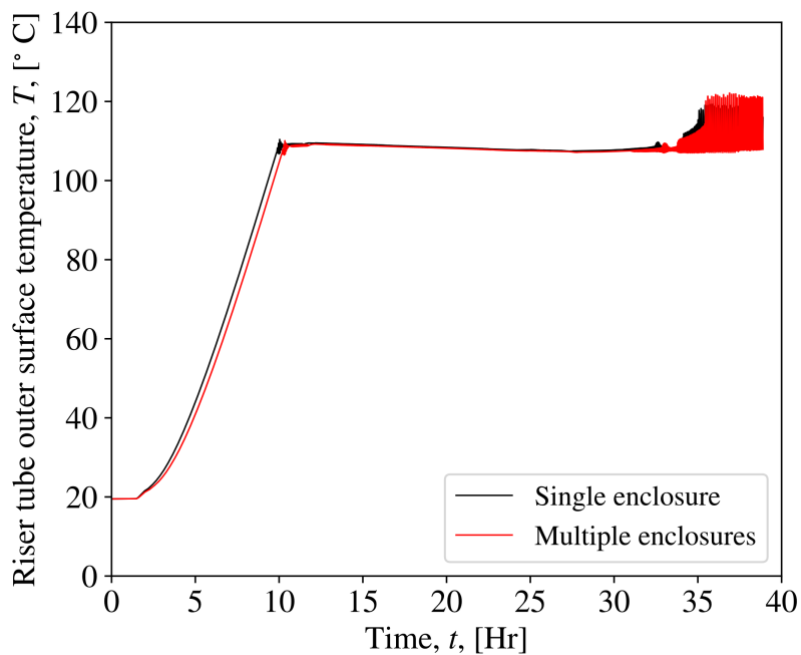


Figure 2-18. Comparison of riser tube outer surface temperature at center of riser tube 4

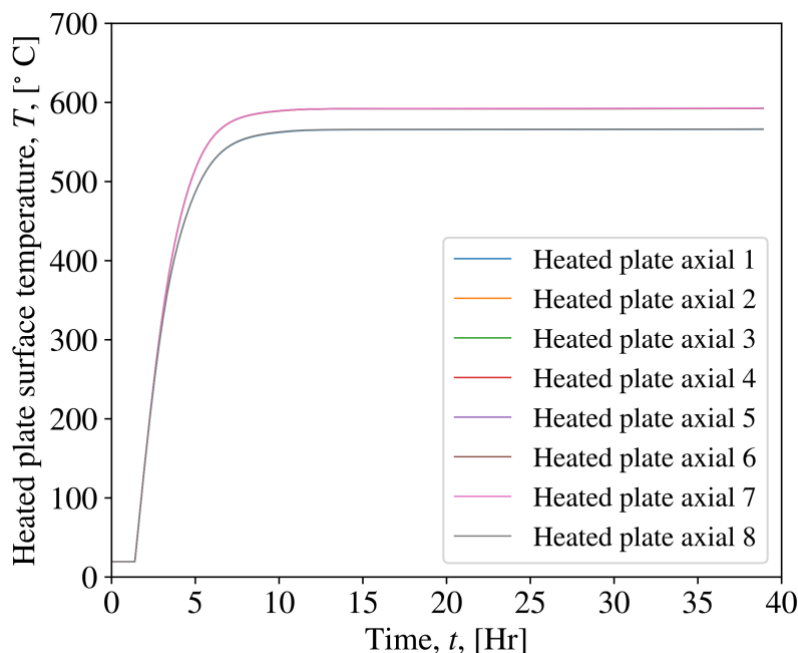


Figure 2-19. Heated plate inner surface temperatures with cavity model 2

2.3 Code Benchmark using Single-phase Test Data

The RELAP5 NSTF model, with the cavity modeled using the single-enclosure approach, is benchmarked with single-phase test data in this section. The benchmark process consists of two steps. In the first step, the NSTF loop behaviors are benchmarked by tuning the form loss coefficients at the elbows and tees. During this benchmark step, the cavity is not included, and the heat flux based on the experimentally measured thermal power input is directly applied to the riser outer surface. In the second step, the air cavity behaviors are benchmarked by tuning the heat transfer coefficients for the heated plate and riser assembly surfaces, the ceramic heater surface emissivity, and the heat loss heat transfer coefficient of the cavity exterior surface. One observation from the cavity modeling study discussed in the previous section is that a symmetric temperature profile is predicted for the heated plate with only radiation heat transfer considered, which is inconsistent with the linear axial temperature distribution obtained from the experiments. Therefore, internal natural convection/circulation was incorporated into the cavity model during the benchmark process. In addition, thermal insulations for the cavity were also considered, with a natural convective heat loss boundary condition applied to the cavity exterior surface.

For the NSTF single-phase matrix testing, a total of four tests with varying thermal powers were conducted. Out of these tests, the single-phase baseline case (Run052) corresponding to the full scale ‘accident scenario’ power of 2.1 MW_t (51.6 kW_t nominal in the test), along with two isothermal characterization tests, was first selected to derive the benchmarked form loss coefficients for the elbows and tees, which are summarized in Table 2-1. Pressure drops measured by two differential pressure transmitters for the chimney sections were used to derive the elbow form loss coefficient. There was no direct way to derive the form loss coefficients for the tees since they were welded together to form the riser inlet and outlet headers and there were no differential pressure transmitters instrumented for an individual tee. The tee form loss

coefficients were tuned until both the riser flow rates and the total test section pressure drop predicted by RELAP5 were within 4% of the test results. With the calibrated form loss coefficients, the Run052 simulation results agree well with the experimental results, as shown in Table 2-2. It should be noted that the highlighted parameters, namely, the thermal power, riser inlet temperature, and HXG flow rate are fixed inputs in the RELAP5 model. The same calibrated form loss coefficients were then applied to the other three single-phase test cases, all yielding good agreement between the simulation and experimental results, shown in Table 2-3 to Table 2-5. The predicted fluid temperatures are within 2.5% of the test results, while the total flow and riser flows within 6%, as shown in Figure 2-20 and Figure 2-21.

Table 2-1. Calibrated form loss coefficient.

	Reference [2-2]	Calibrated
Elbow	0.39	0.22
Tee through	0.19	0.10
Tee branch	0.80	0.62

Table 2-2. Benchmarked NSTF loop results for single-phase test Run052.

	Exp	Sim	Diff	%Diff
Power, kW_t	51.81	51.81	0.00	0.00%
Riser inlet, °C	30.37	30.37	0.00	0.00%
Riser outlet, °C	39.64	39.64	0.00	-0.01%
Tank inlet, °C	39.67	39.62	-0.05	-0.13%
Tank outlet, °C	30.38	30.38	0.00	0.00%
HXG hot supply, °C	30.61	30.39	-0.22	-0.71%
HXG hot return, °C	11.48	11.40	-0.08	-0.66%
HXG flow, kg/s	0.65	0.65	0.00	0.00%
System flow, kg/s	1.338	1.336	-0.002	-0.13%
Riser 1, kg/s	0.169	0.164	-0.006	-3.46%
Riser 2, kg/s	0.161	0.164	0.003	1.68%
Riser 3, kg/s	0.164	0.165	0.001	0.56%
Riser 4, kg/s	0.166	0.166	0.000	-0.13%
Riser 5, kg/s	0.170	0.167	-0.002	-1.42%
Riser 6, kg/s	0.168	0.168	0.000	0.18%
Riser 7, kg/s	0.165	0.170	0.005	2.75%
Riser 8, kg/s	0.177	0.172	-0.005	-2.85%

Table 2-3. Benchmarked NSTF loop results for single-phase test Run051.

	Exp	Sim	Diff	%Diff
Power, kW_t	33.73	33.73	0.00	0.00%
Riser inlet, °C	30.74	30.74	0.00	0.00%
Riser outlet, °C	37.82	37.82	-0.01	-0.01%
Tank inlet, °C	37.85	37.80	-0.05	-0.13%
Tank outlet, °C	30.74	30.75	0.02	0.06%
HXG hot supply, °C	30.98	30.77	-0.21	-0.67%
HXG hot return, °C	17.17	17.38	0.21	1.20%
HXG flow, kg/s	0.60	0.60	0.00	0.00%
System flow, kg/s	1.140	1.138	-0.002	-0.18%
Riser 1, kg/s	0.145	0.139	-0.005	-3.74%
Riser 2, kg/s	0.138	0.140	0.002	1.76%
Riser 3, kg/s	0.140	0.141	0.000	0.18%
Riser 4, kg/s	0.142	0.141	0.000	-0.10%
Riser 5, kg/s	0.144	0.142	-0.002	-1.09%
Riser 6, kg/s	0.143	0.143	0.000	0.33%
Riser 7, kg/s	0.141	0.145	0.004	2.68%
Riser 8, kg/s	0.150	0.146	-0.004	-2.94%

Table 2-4. Benchmarked NSTF loop results for single-phase test Run054.

	Exp	Sim	Diff	%Diff
Power, kW_t	16.51	16.51	0.00	0.00%
Riser inlet, °C	29.47	29.47	0.00	0.00%
Riser outlet, °C	34.06	34.06	0.00	0.01%
Tank inlet, °C	34.08	34.04	-0.04	-0.13%
Tank outlet, °C	29.49	29.49	0.00	-0.01%
HXG hot supply, °C	29.88	29.50	-0.38	-1.27%
HXG hot return, °C	12.47	12.78	0.31	2.49%
HXG flow, kg/s	0.23	0.23	0.00	0.00%
System flow, kg/s	0.861	0.856	-0.005	-0.55%
Riser 1, kg/s	0.111	0.105	-0.006	-5.61%
Riser 2, kg/s	0.103	0.105	0.003	2.58%
Riser 3, kg/s	0.108	0.106	-0.002	-2.17%
Riser 4, kg/s	0.107	0.106	-0.001	-0.69%
Riser 5, kg/s	0.110	0.107	-0.003	-2.54%
Riser 6, kg/s	0.108	0.108	0.000	-0.40%
Riser 7, kg/s	0.107	0.109	0.002	2.07%
Riser 8, kg/s	0.114	0.110	-0.004	-3.53%

Table 2-5. Benchmarked NSTF loop results for single-phase test Run055.

	Exp	Sim	Diff	%Diff
Power, kW_t	61.14	61.14	0.00	0.00%
Riser inlet, °C	30.67	30.67	0.00	0.00%
Riser outlet, °C	40.90	40.91	0.00	0.01%
Tank inlet, °C	40.94	40.89	-0.05	-0.13%
Tank outlet, °C	30.68	30.69	0.01	0.02%
HXG hot supply, °C	30.81	30.70	-0.12	-0.39%
HXG hot return, °C	17.08	16.93	-0.16	-0.92%
HXG flow, kg/s	1.06	1.06	0.00	0.00%
System flow, kg/s	1.431	1.428	-0.003	-0.20%
Riser 1, kg/s	0.182	0.175	-0.007	-3.80%
Riser 2, kg/s	0.174	0.175	0.002	0.93%
Riser 3, kg/s	0.185	0.176	-0.009	-4.62%
Riser 4, kg/s	0.180	0.177	-0.002	-1.24%
Riser 5, kg/s	0.189	0.179	-0.010	-5.31%
Riser 6, kg/s	0.180	0.180	0.000	-0.15%
Riser 7, kg/s	0.176	0.182	0.005	3.05%
Riser 8, kg/s	0.190	0.183	-0.007	-3.67%

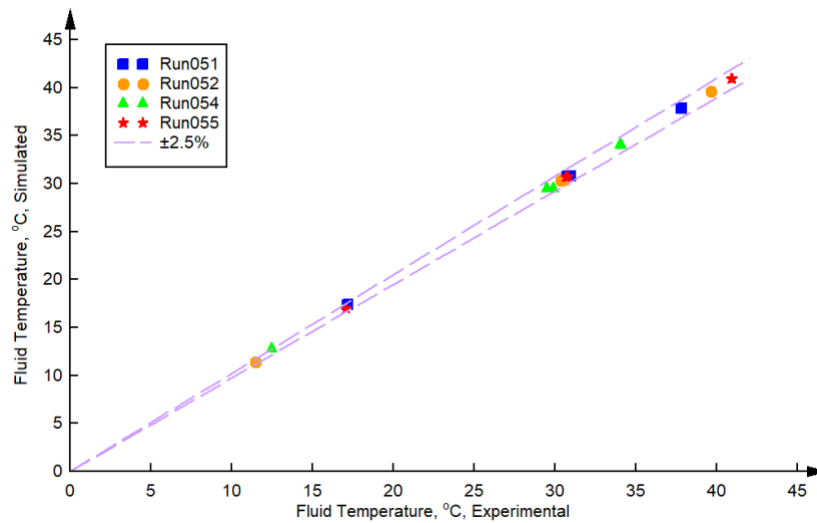


Figure 2-20. Benchmark results for the loop behaviors, fluid temperatures.

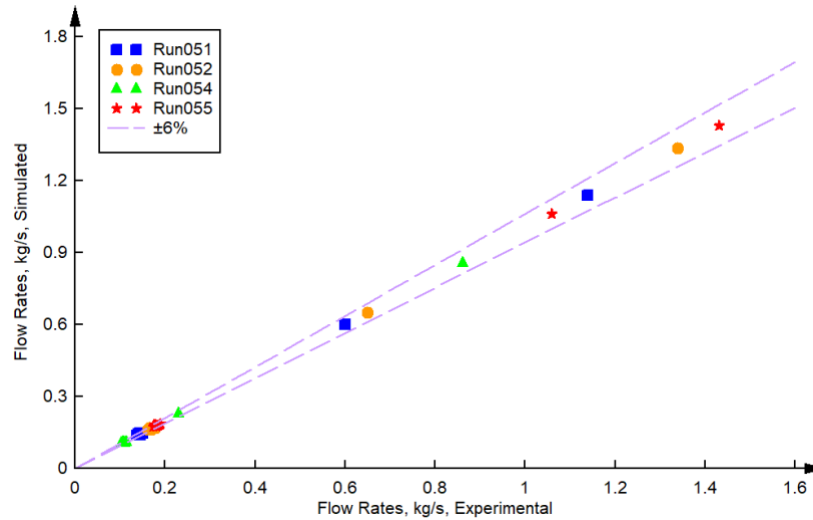


Figure 2-21. Benchmark results for the loop behaviors, flow rates.

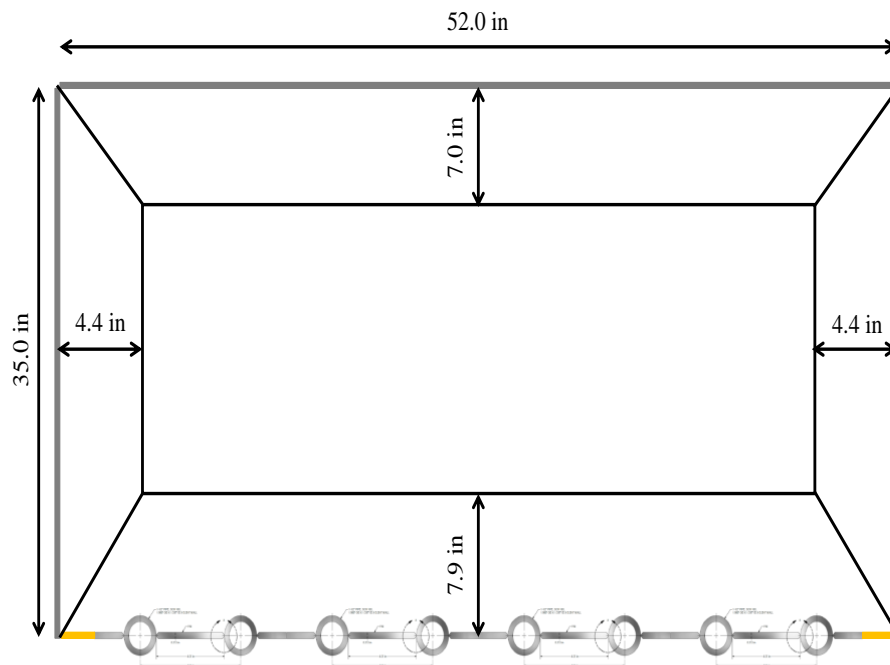


Figure 2-22. Flow passages modeled for the cavity internal natural convection/circulation.

In the second portion of the benchmark study, the modeling focus was on air cavity behaviors, specifically the heated plate temperatures, heater temperatures, and cavity outer surface temperatures. The modeled cavity consists of the riser assembly, heated plate, and cavity walls. Two heat transfer mechanisms are considered in the present model, namely, the radiation heat transfer and the internal natural convection/circulation. For the radiation heat transfer, the riser assembly, heated plate, and the side walls are each axially divided into eight vertical layers, resulting in a total of 98 surfaces that are modeled within one radiation enclosure. The required inputs of view factors are calculated from the CFD simulations. For the internal natural convection/circulation, four axial flow passages next to the heated plate, the cooling panel, and the side walls are employed by referring to CFD analysis results, as shown in Figure 2-22. In

addition to the natural convective heat loss on the outer surface of the cavity walls, potential heat loss through the air gap between the heated plate and ceramic heaters is also considered. Both convective and radiative heat transfers through this air gap were simulated. The single-phase test case of Run052 was selected for this benchmark study. The benchmark process was focused on three aspects: 1) the cavity internal natural convective heat transfer due to the additional curvatures in the riser assembly induced by the round riser tubes; 2) the heater surface emissivity; 3) the external natural convection heat loss due to the large uncertainties observed in literature.

The process of tuning the parameters is performed in three separate steps. In the first step, the natural convection heat transfer coefficient of the riser assembly surface is tuned to match the predicted heated plate temperature with the experimental data. As the heat transfer coefficient is calculated internally by the code, tuning is done by adjusting the fouling factor. The results are shown in Figure 2-23 where the heated plate temperature decreases as the fouling factor increases due to the increase of the heat transfer capability of the riser assembly. The heated plate temperature is observed to decrease slightly non-linearly with respect to the fouling factor.

Given that the rate of natural convection in the cavity is affected by both the riser surface temperature and the heated plate surface temperature, the same process is repeated by tuning the fouling factors of the heat transfer coefficients of both surfaces. To avoid further complication, the fouling factors of both surfaces are kept the same in the tuning process. The results are shown in Figure 2-24 where the heated plate temperature is observed to decrease almost linearly with respect to the fouling factor. Note that the values of the fouling factors range only from 1.1 to 1.4, which is smaller than the values in the previous exercise of 1.1 to 2.1. As the current approach tunes the heat transfer coefficients of both the riser and heated plate surfaces, it takes a smaller fouling factor to have an equal impact on the heated plate temperature than the previous exercise. Based on the results, a fouling factor of 1.24 is required for the heat transfer coefficients of the heated plate and riser surfaces to match the simulated heated plate temperature to the experimental data.

With the predicted heated plate temperature matching the experimental value, the second step involves the tuning of the heater emissivity to match the predicted heater temperature to the experimental value. In the heater assembly, the heated plate and the heater are separated by an air gap with a width of 4.7625 mm (3/16”), and heat is transferred from the heater to the heated plate via thermal radiation. Thus, the emissivity of the heater surface has a direct impact on the heat transfer capability between these two surfaces and consequently the overall temperature of the heater. Note that the surface of the heater is protected by a thin stainless-steel 304 covering sheet, thus the surface emissivity of stainless-steel 304 is used as the default value. The results are shown in Figure 2-25 where the average heater temperature decreases slightly non-linearly as the heater surface emissivity increases due to the improved heat transfer between the heater and the heated plate. The results show that with a heater surface emissivity of 0.317, the predicted average heater temperature matches the experimental value the best.

Now that the predicted average heated plate and heater temperatures match the experimental values, the heat transfer coefficient of the heat loss at the cavity external surface is tuned to match the predicted cavity exterior temperature to the experimental value. Even though the cavity is well insulated, some heat loss to the environment is inevitable. The default value of the

heat loss heat transfer coefficient is determined using the empirical correlation for natural convection for vertical plates as suggested by Cengel [2-5]. The value of the heat loss heat transfer coefficient is tuned by multiplying the default values with different values of enhancement factor. The results are shown in Figure 2-26 where the predicted cavity exterior temperature decreases linearly with the increase of the enhancement factor. It is observed that the heat loss heat transfer coefficient needs only to be increased by 8.4% (enhancement factor of 1.084) for the predicted cavity exterior temperature to match the experimental value. With the model tuned according to the experimental data, the predicted steady-state cavity temperatures agree well with the testing results, as shown in Table 2-6. The improved and tuned RELAP5 model is then benchmarked with transient experimental data and the results are discussed in next section.

It is worth pointing out that the average heater temperature can also be tuned with a different approach than the approach discussed previously (Step 2). As highlighted earlier, the surface of the heater is covered with a thin sheet of stainless-steel 304 for protection. As the stainless-steel sheet and the heater surface may not be in perfect contact with each other, there exists an inherent contact resistance that inhibits the heat transfer between these two components, which will lower the effective thermal conductivity of the heater and the cover sheet. Consequently, the decrease in the overall heat transfer capability of the heater-cover sheet pair can be modeled by introducing a reduction factor to the thermal conductivity of the heater. The results are shown in Figure 2-27 where the average heater temperature decreases exponentially with the increase of the reduction factor due to the improved heat conduction capability.

Table 2-6. Benchmarked steady-state cavity temperatures with a riser and heated plated heat transfer fouling factor of 1.24, a heater surface emissivity of 0.317, and a cavity exterior heat loss coefficient enhancement factor of 1.084.

	Experiment	RELAP5	% Diff
Heated Plate Average Temperature, °C	403.73	403.61	-0.03%
Heater Average Temperature, °C	573.30	573.52	0.04%
Cavity Exterior Temperature, Upper East, °C	75.00	74.95	-0.07%

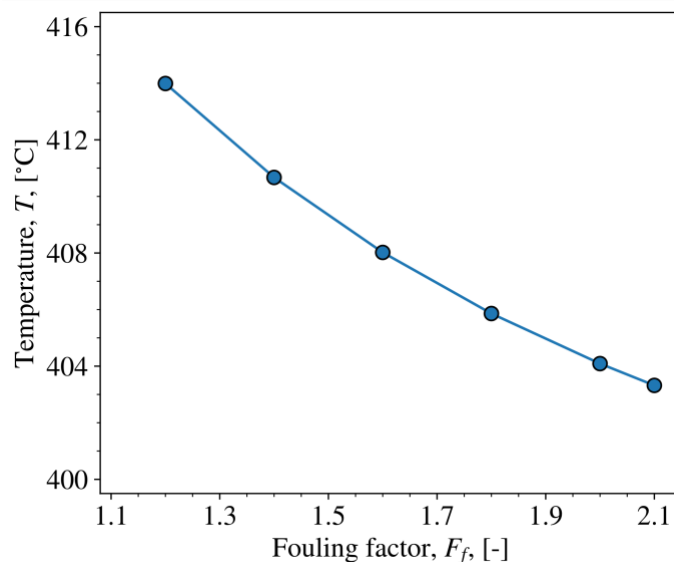


Figure 2-23. Comparison of the predicted average heated plate temperatures with respect to fouling factors of only the riser surface natural convection heat transfer coefficient.

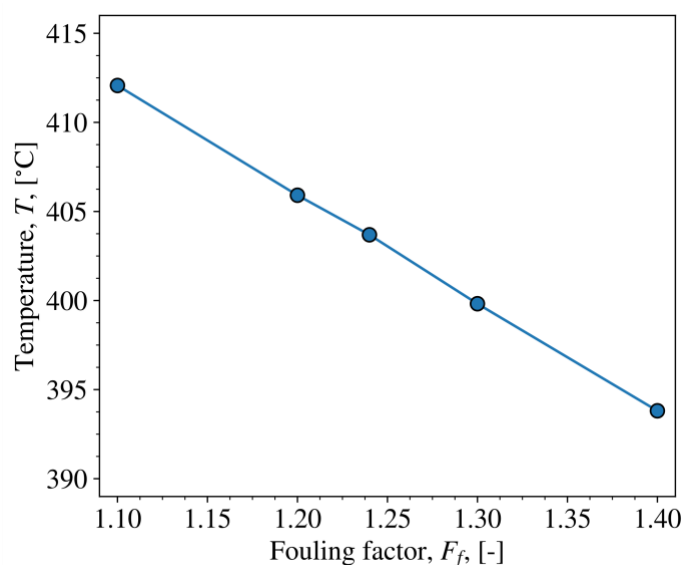


Figure 2-24. Comparison of the predicted average heated plate temperatures with respect to fouling factors of both the riser surface and the heated plate surface natural convection heat transfer coefficient.

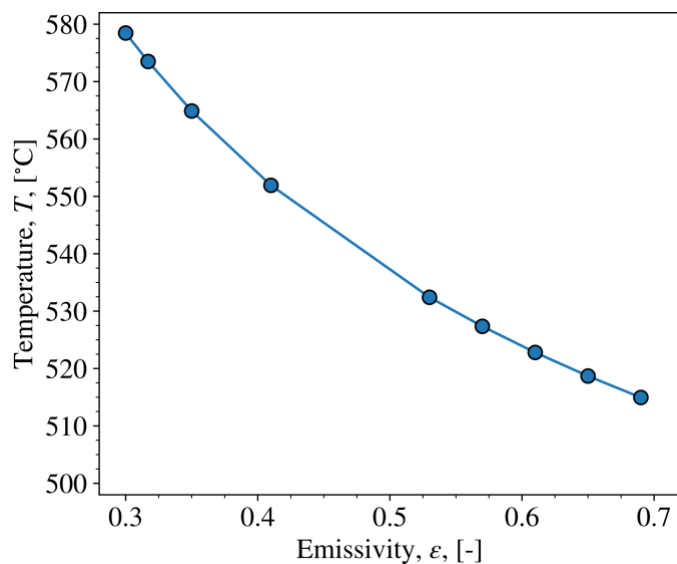


Figure 2-25. Comparison of the predicted average heater temperatures with respect to the heater surface emissivity.

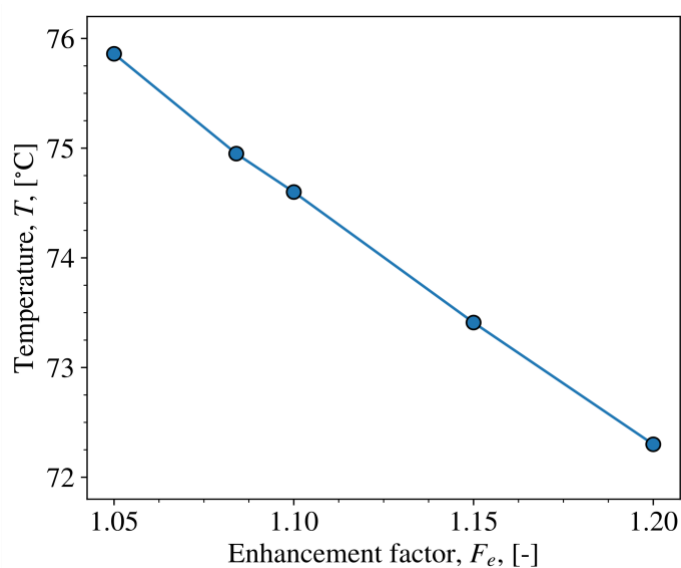


Figure 2-26. Comparison of the predicted cavity exterior temperatures with respect to the enhancement factors of the heat loss heat transfer coefficient.

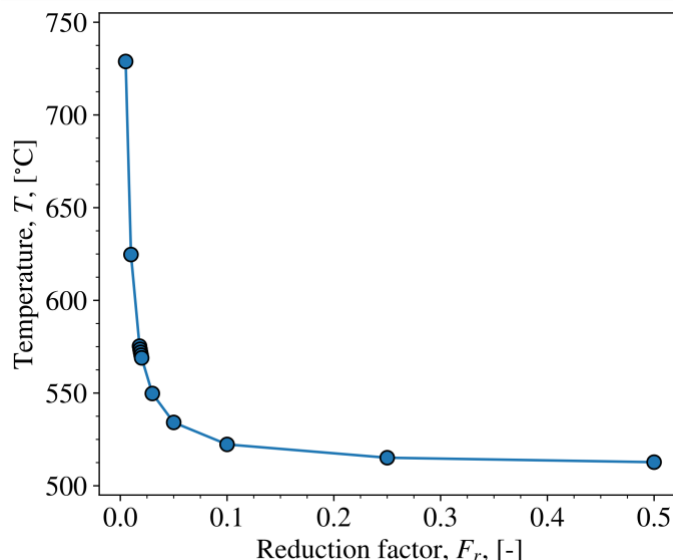


Figure 2-27. Comparison of the predicted average heater temperatures with respect to the reduction factors of the heater thermal conductivity.

2.4 Code Benchmark using Transient Test Data

With the steady-state loop and cavity behaviors benchmarked, the calibrated parameters including the loop flow resistance coefficients, cavity heat transfer enhancement factors, and the heater surface emissivity were applied to the transient RELAP5 simulation for test case of Run052. The initial fluid and structure temperatures, initial flow rates, heater power, cooled inventory returning temperature and flow rate are the initial and boundary conditions specified with reference to the experimental results. The predicted system transient behaviors in comparison with the experimental results are shown in Figure 2-28 to Figure 2-30. As seen, the experimental results and simulation results converge at the steady state, which is understandable since the tuned parameters are based on steady state results. For the first ~ 3 hours, the simulation results agree well with the experimental results, especially the heater temperatures and the initiation of the system wide natural circulation. Following that, however, the predictions start to deviate from the experimental results.

The over prediction of the flow rate, fluid temperatures, and heater temperatures indicate that the transient heat loss is underestimated. Currently, two heat loss mechanisms are considered, namely, the conduction heat loss through the thermal insulations and the heat loss due to leak air flow in the heater-plate gap. The first is the result of steel structural used to support the large weight of the heated plate; components necessary to the construction but result in the new paths for conduction heat loss. The second is caused by the high surface temperatures and leakages in porous insulation, which together allow external natural convection to develop into small air flows and cause additional parasitic heat loss. Both mechanisms are artifacts of the large scale of the experimental facility, and difficult to quantify with measurements. Thus, best estimates were made using 1D conduction and material properties of support structures, along with tuned estimates of leakage air flow rate. The leak air flow is already well developed by ~ 3 hours, Figure 2-31, indicating full contribution to the heat loss. Therefore, the conduction heat loss has

been likely underestimated. The discrepancy observed in the transient simulation suggests possible improvements are necessary for heat loss portion of the model.

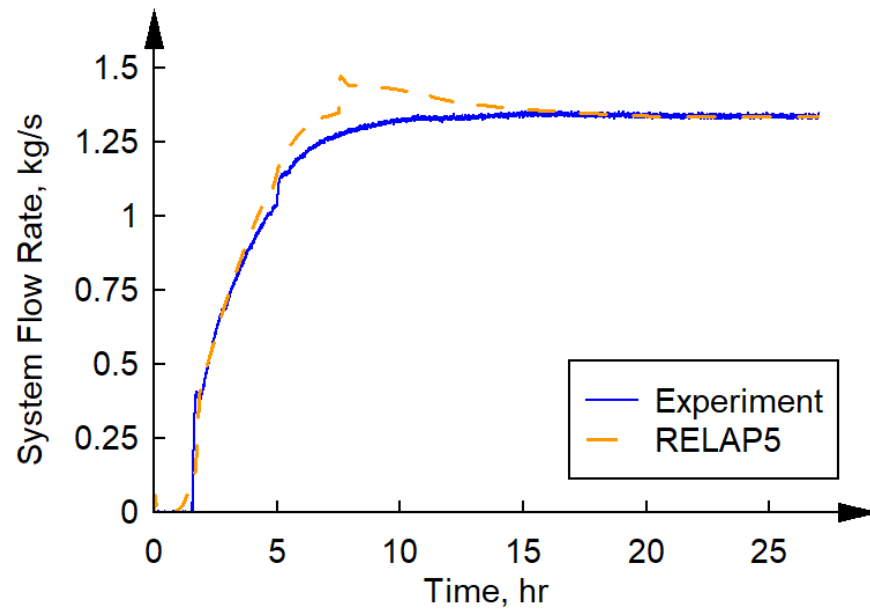


Figure 2-28. System flow rate.

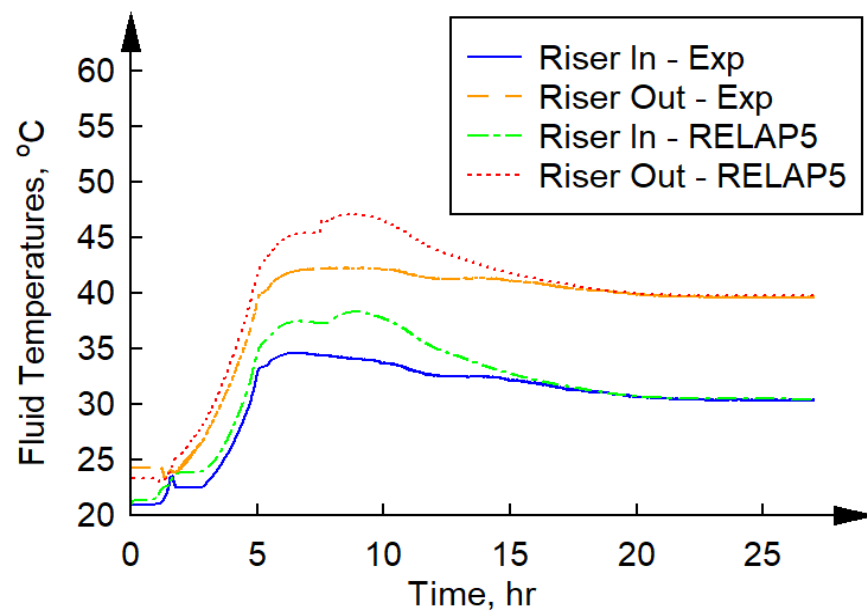


Figure 2-29. Test section inlet/outlet temperatures.

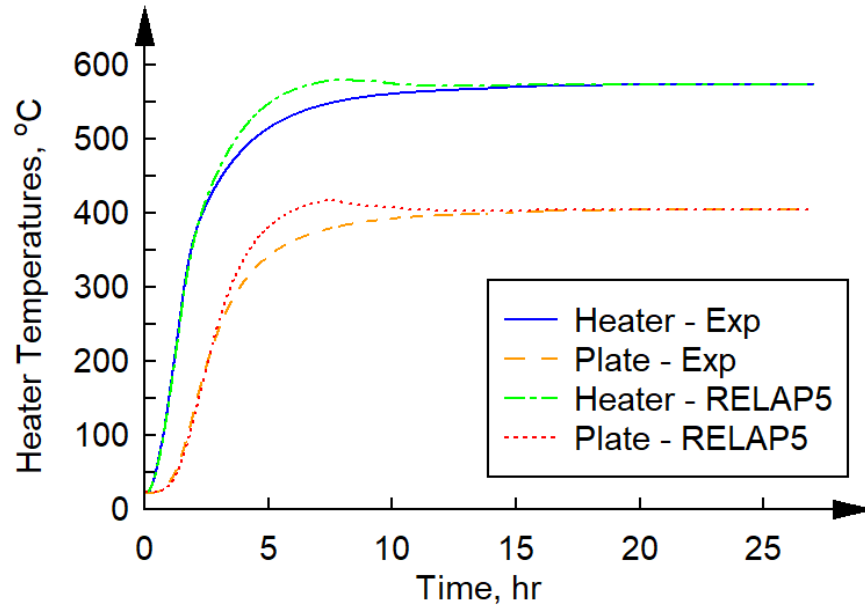


Figure 2-30. Heater temperatures.

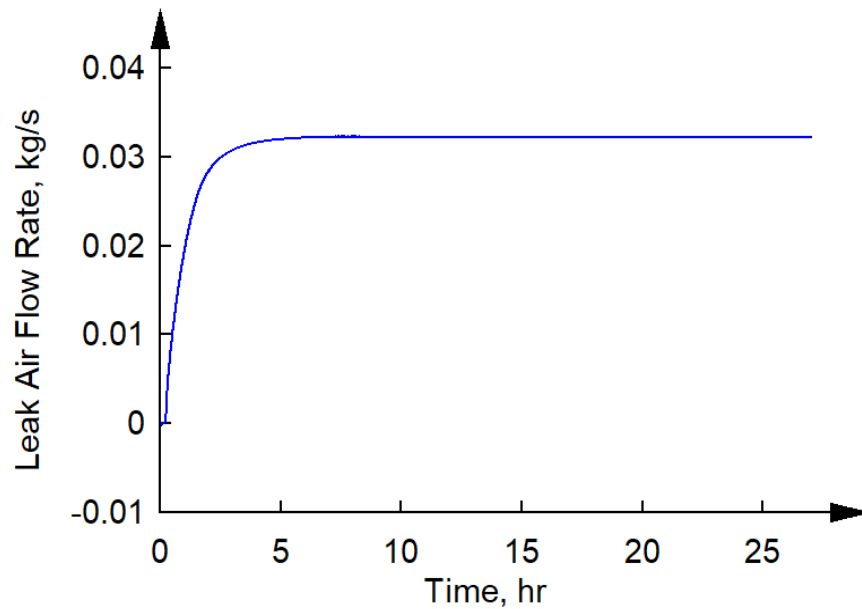


Figure 2-31. Leak air flow from RELAP5 model.

2.5 Code comparison between RELAP5-3D and RELAP5-MOD3.3

In the current RELAP5 model for the water based NSTF, each riser tube and its corresponding fins are assumed as one unit slab, and convective boundary is applied directly between the slab and the water inside the riser tube. This neglects the thermal conduction process in the fins and thus underestimates the thermal resistance in the heat transfer process. So far, all the two-phase simulations have been performed with RELAP5-MOD3.3 due to its capability in predicting low-pressure two-phase flow instabilities as frequently mentioned in literature.

However, MOD 3.3 does not include the capability of conduction enclosure. RELAP5-3D, on the other hand, has the conduction enclosure capability. Before adopting RELAP5-3D to simulate the radial thermal conduction in the riser tube fins, its capability in simulating the water based NSTF, especially the flow instabilities characteristic of low-pressure boiling, needs to be evaluated.

The two-phase baseline case was simulated with RELAP5-3D, with exactly the same input as with MOD3.3. Figure 2-32 shows a comparison in the total system flow predicted by the two codes. As can be seen, the single-phase flow predicted by the two codes is quite similar. However, RELAP5-3D appears to predict a higher system flow during the two-phase transient than RELAP5-MOD3.3. Furthermore, RELAP5-3D would predict less two-phase flow oscillations due to either the density wave oscillations or geysering. Efforts were made to identify causes of the differences in the predicted system flow by the two codes. Specifically, the following development options, shown in Table 2-7, that are implemented by default in RELAP5-MOD3.3 but not in RELAP5-3D were investigated.

According to the RELAP5-3D user's guide [2-3], Option-55 is a collection of modeling improvements designed to minimize numerical sources of oscillations for low pressure two-phase flow simulations, which particularly affects the interfacial heat transfer for annular mist, mist pre-CHF, and mist post-CHF flow regimes. With this option, physical models replace the ad-hoc correlations used for modeling the liquid-side interfacial heat transfer coefficient. Option-57 modifies the phasic partitioning of the wall friction so that all the wall friction is applied to the liquid film in the annular mist flow regime. This option is necessary for the computation of realistic values of the liquid film thickness. Option-58 changes the smoothing used for the bubbly flow liquid interfacial heat transfer coefficient between the liquid superheat and liquid subcooled regions. Lastly, Option-61 further modifies constitutive relationships to reduce numerical oscillations at low pressure. This option specifically affects the vertical stratification model and the interfacial heat transfer model for bubbly and slug flow regimes.

Table 2-7. RELAP5 3D options descriptions.

Options	Descriptions
55	Low Press Modeling Improvements
57	Annular Mist Wall Friction
58	Bubbly Flow Smoothing
61	Low Press Modeling Mods

The effects of these development options on the predicted total system flow are shown in Figure 2-32. As can be seen, with Option-61, RELAP5-3D agrees well with MOD3.3 in predicting the total system flow. However, the other options have negligible effect on the predicted total system flow by RELAP5-3D. In addition, none of these options enables RELAP5-3D to capture the flow instabilities.

In addition to the differences in modeling options, RELAP5-MOD3.3 and 3D use different algorithms as the linear-equation solver for solving the hydrodynamic equations. RELAP5-MOD3.3 uses the Lower-Upper (LU) decomposition solver while RELAP5-3D uses the Border-Profile Lower Upper (BPLU) solvers as the default option. In RELAP5-3D, the

algorithm can be switched from the default BPLU solver to the iterative Generalized Minimal Residual Method (GMRES) solver by activating Option-34. Using RELAP5-MOD3 and RELAP5-3D Filho et al. [2-4] investigated the impact of the differences in the solver algorithms for a two-phase natural circulation loop. According to Filho et al. [2-4], the simulation results from the three algorithms showed excellent agreement when the flow was in single-phase. Conversely, when the flow was undergoing two-phase instabilities, significant discrepancies were observed where the LU solver predicted instabilities with a shorter wavelength than the BPLU and GMRES solvers. The results from the BPLU solver were also reported to agree well with the results from the GMRES solver. Besides, the oscillations from the LU solver have a more uniform pattern than the oscillations from the BPLU and GMRES solvers. Effort of investigating the effects of the differences between the solvers on the NSTF model is still ongoing.

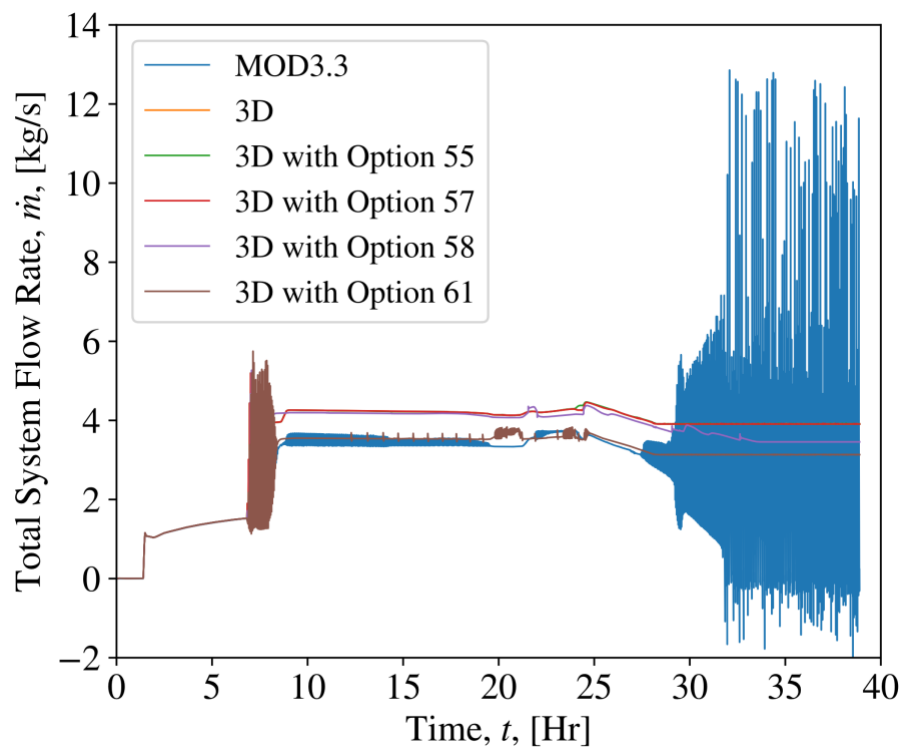


Figure 2-32. Comparison between RELAP5-3D and MOD 3.3 in predicting the total system flow for the two-phase baseline case.

2.6 Summary and Future Work

The Natural convection Shutdown heat removal Test Facility (NSTF) at Argonne National Laboratory was built to study the performance of passive systems for advanced nuclear reactors. This section documents the FY21 progress and achievements made in the system level analysis of the NSTF with the thermal hydraulics code, RELAP5. As a continuation of progress reported in FY17, the RELAP5 model of the NSTF is updated in this report to include the modeling of the cavity. Two different cavity models are developed, one that models the radiation heat exchange among all surfaces in one enclosure (Cavity Model 1), and another that employs multiple

radiation enclosures with each considering the surfaces at one axial level (Cavity Model 2). Results from CFD analysis are used to obtain the view factors for both models.

In order to benchmark the cavity models, they are used for simulating a two-phase baseline case. Comparing the RELAP5 model with Cavity Model 1 to the model without the cavity, a good agreement is obtained between the two sets of results. With the consideration of the cavity, a slower transient is predicted primarily due to the increased thermal inertia from the cavity and the additional thermal resistance corresponding to the thermal radial process. However, the predicted durations of the transient and the mass flow rates during the quasi-steady state after the transient from both sets of simulations are in a good agreement with each other. Analyses of other parameters such as the riser tube outer surface temperatures, the heat flux distribution on the riser surface, and the temperature distribution on the heater surface also show that the behaviors of these parameters are consistent with the expectations. The predictions from Cavity Model 1 are also compared with those from Cavity Model 2 where an excellent agreement is obtained. The onset of transient is predicted slightly later with Cavity Model 2 due to the increased thermal resistance caused by the larger number of enclosures, which also results in a higher temperature on the inner surface of the heated plate. Consequently, Cavity Model 1 is used for modeling the cavity for the remainder of the work as it is more physical than Cavity Model 2.

The NSTF RELAP5 model is then benchmarked using single-phase test data from four experimental conditions with varying thermal powers with a two-step approach. In the first step, using a single-phase baseline case as the reference, the form loss coefficients of the elbows and tees are first tuned. The tuned model can accurately predict the fluid temperatures to within 2.5% of the experimental data, and the total and riser flow rates to within 6%. On the other hand, the second step of the benchmark focuses on the thermal behavior of the cavity. The natural convection heat transfer coefficients of the riser and heated plate surfaces in the cavity, the emissivity of the heater, and the heat transfer coefficient of heat loss on the exterior of the cavity are tuned to match the average heated plate temperature, the average heater temperature, and the cavity exterior temperature to the experimental measurements. The tuned model can predict these three parameters to an excellent accuracy with respect to the experimental data.

The tuned RELAP5 model is then benchmarked with transient data in the next step. The predictions agree well with the experimental measurements in the initial phase of transient but start to deviate roughly 3 hours from the beginning of the simulation. The overprediction of the flow rate, fluid temperatures, and heater temperatures indicate that the transient heat loss is underestimated. However, as the system starts to stabilize, the predictions and the experimental measurements once again agree with each other.

Lastly, a code-to-code comparison is performed to investigate the differences in the capabilities of RELAP5-MOD3.3 and RELAP5-3D to simulate two-phase flow instabilities. The single-phase predictions by both versions of RELAP5 agree well with each other but significant differences are observed in the two-phase predictions where the default RELAP5-3D run did not capture either the density wave oscillations or geysering. Various user options in RELAP5-3D are explored with Option-61 (modifications on constitutive relations under low-pressure conditions) yielding satisfactory results.

For future steps, efforts are currently underway to investigate RELAP5-3D's poor performance in predicting low-pressure two-phase instabilities. Next, a more accurate model of the assembly of riser tubes and fins, with the consideration of the thermal conduction in the fins, will be implemented.

References

- [2-1] Lv, Q., Kraus, A., Hu, R., Bucknor, M., Lisowski, D., & Nunez, D. (2017). Progress Report on Computational Analyses of Water-Based NSTF. ANL-ART-103, Argonne National Laboratory.
- [2-2] Hydraulic Institute (1961). Pipe Friction Manual.
- [2-3] The RELAP5-3D Code Development Team (2015). RELAP5-3D Code Manual Volume II: User's Guide and Input Requirements. INL/MIS-15-36723, Idaho National Laboratory.
- [2-4] Filho, F. A. B., Sabundjian, G., Ribeiro, G. H., & Caldeira, A. D. (2017). Assessment of RELAP5 matrix solvers for a two-phase natural circulation loop. *Annals of Nuclear Energy*, 105 (207), pp. 249-258.
- [2-5] Cengel, Y. A., (2002). *Heat Transfer: A Practical Approach*, Second Edition. McGraw-Hill Education.

3 CFD Analyses of Water-Cooled NSTF

3.1 CFD Model Description

Prior CFD analyses of the water-cooled NSTF were largely focused on the heated cavity, and recent work has continued exploring this area of the flow domain. Given the fact that two-phase phenomena are not anticipated in the vicinity of the risers for most transients, the cavity should be a region in which CFD can readily and confidently make contributions to the understanding of key flow phenomena. However, expanding the scope to the full water-cooled system is non-trivial. Unlike in the air-cooled system, which had a clear geometric inlet/outlet structure to the NSTF experimental apparatus, the water-cooled system is a loop, with boundary and flow conditions that are not as straightforward to model in CFD. This would require significant testing to confidently include modeling results from the other portions of the domain where two-phase flow may occur.

In an effort to broaden the potential scope of the CFD analysis domain beyond just the heated cavity, a CAD model was built that attempts to model the entire primary water flow path (Figure 3-1). This includes the riser tubes, fins, water, insulation, and air in the cavity region. New additions are the inlet and outlet headers to/from the cavity region, associated piping, and water storage tank. Note that only the water portion, i.e., no solids, is modeled outside of the cavity region.

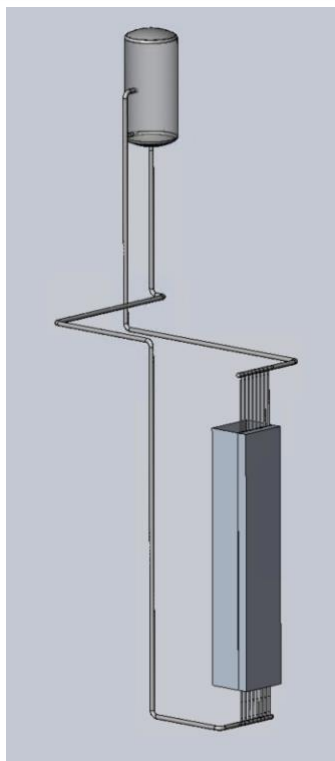


Figure 3-1. CAD geometry of the primary water-cooled NSTF flow path, including the heated cavity.

Note that the full CAD need not be used for all simulations; in fact, it is often practical to isolate the computational domain to certain areas that demonstrate clear three-dimensional flow behavior, and use approximate boundary conditions. For the NSTF, this primarily includes the heated cavity, inlet and outlet headers, and water storage tank. The meshes and models varied depending on the exact problem being solved, and are described in the case-specific sections below. All comparisons against experimental data were performed for Run052, a steady-state, single-phase test.

The methods employed in the following simulations are largely based upon those in prior reports [3-1]. STAR-CCM+ v15.06 [3-2] is used to perform the analyses. Two notable changes were made to the heated cavity setup as compared with prior runs. First, it was established that the upper and lower surfaces of the heated cavity were changed from the air system to be very shiny, with emissivities of 0.005 assumed. Also, it was initially assumed that the centerline of the tubes in the water-cooled system was at the same distance from the heated surface as the centerline of the ducts in the air-cooled system. However, through discussion and examination of the system, it was found that the tubes are actually roughly 2" further from the heated surface than previously assumed. This was changed in the heated cavity CFD model and is reflected in all the results presented here.

3.2 Stand-alone Cavity Modeling

A large portion of the CFD effort was focused on describing the characteristics of flow within the heated cavity. As compared to the air, the cavity modeling for the water system was

initially presumed to be “simpler”; the cavity walls and the combined tube/fin panel represent relatively flat and uniform surfaces such that more regular natural convection flow could likely be established. It was shown in practice that nuances of the modeling and boundary conditions required some additional studies, which are detailed here.

A major difference between the air and water systems is that the air system has a completely “open” cavity; the heated wall can “see” the opposite colder wall and they interact through (predominantly) radiation heat transfer. However, the riser/tube panel in the water system is opaque and nearly completely separates the cavity into two domains, a “hot side” and a “cold side”, such that there is intended to be no direct radiation heat transfer between the heated wall and the cold wall. There is some additional space at the two edges of the cooling panel which is closed by a strip of insulation on either side.

One notable feature of the heated cavity model, initialized with the air model but propagated on to the water as well, is the usage of an adiabatic boundary condition at the side and top walls of the cavity. The heat transfer to the coolant is achieved by then setting the heated plate boundary condition as the heat flux which yields the measured experimental thermal power. The adiabatic side/top wall condition was found to yield generally accurate trends in the wall temperatures, and good results in the coolant temperature distribution. While some prior investigations were performed regarding the usage of varying thermal resistances, etc., on the different walls to try to better match temperature readings throughout the cavity by better representing the insulation resistance, it was found that simple variants of this approach did not offer substantial or straightforward improvement. Thus, the adiabatic approximation was deemed sufficient for the air model, and was used as the starting point in the water model. These simulations also used the assumption of equal pressure at the inlet/outlet of each tube, e.g. no direct impact of the header geometry. The header impact is non-trivial and will be discussed in Section 3.2.3.

The initial simulations performed using this adiabatic approach showed large discrepancies in the cavity wall temperatures and trends, notably for the cold wall. In the initial model comparisons shown in Figure 3-2, the side insulation was initially assumed to be both opaque to radiation and solid, such that it did truly separate the cavity into two separate domains with no circulation between them. While there is still technically conduction through the fins/tubes/insulation to the cold side, this was found to be low, such that radiation and natural circulation in the cold side of the cavity were small. Figure 3-3 shows that these approximations greatly underestimate the slope of the temperature increase on the cold wall. In this figure, generally speaking, the cavity position increases laterally and then axially with increasing TC number. Since the inlet temperature is known and heat transfer is low at the bottom of the cavity, the cold wall temperature predictions are accurate in that region. However, a discrepancy builds with increasing axial distance.

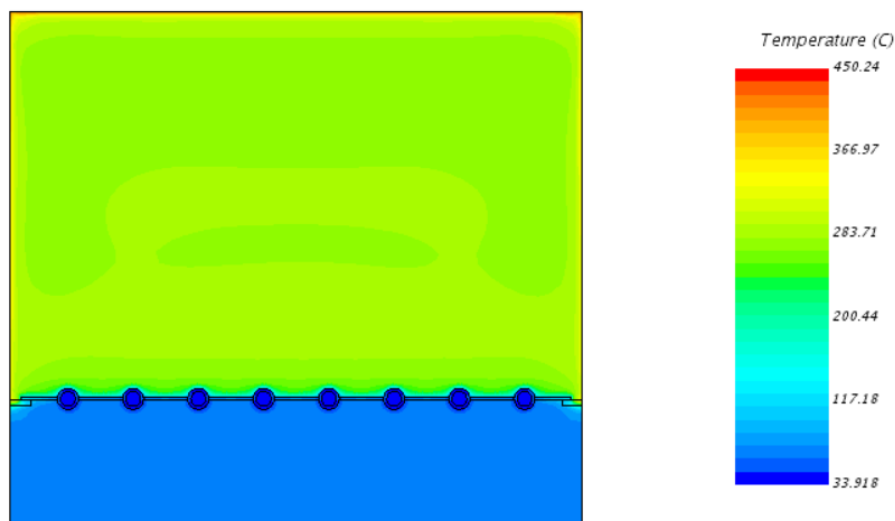


Figure 3-2. Temperature distribution at the midplane of the heated cavity for the initial simulation.

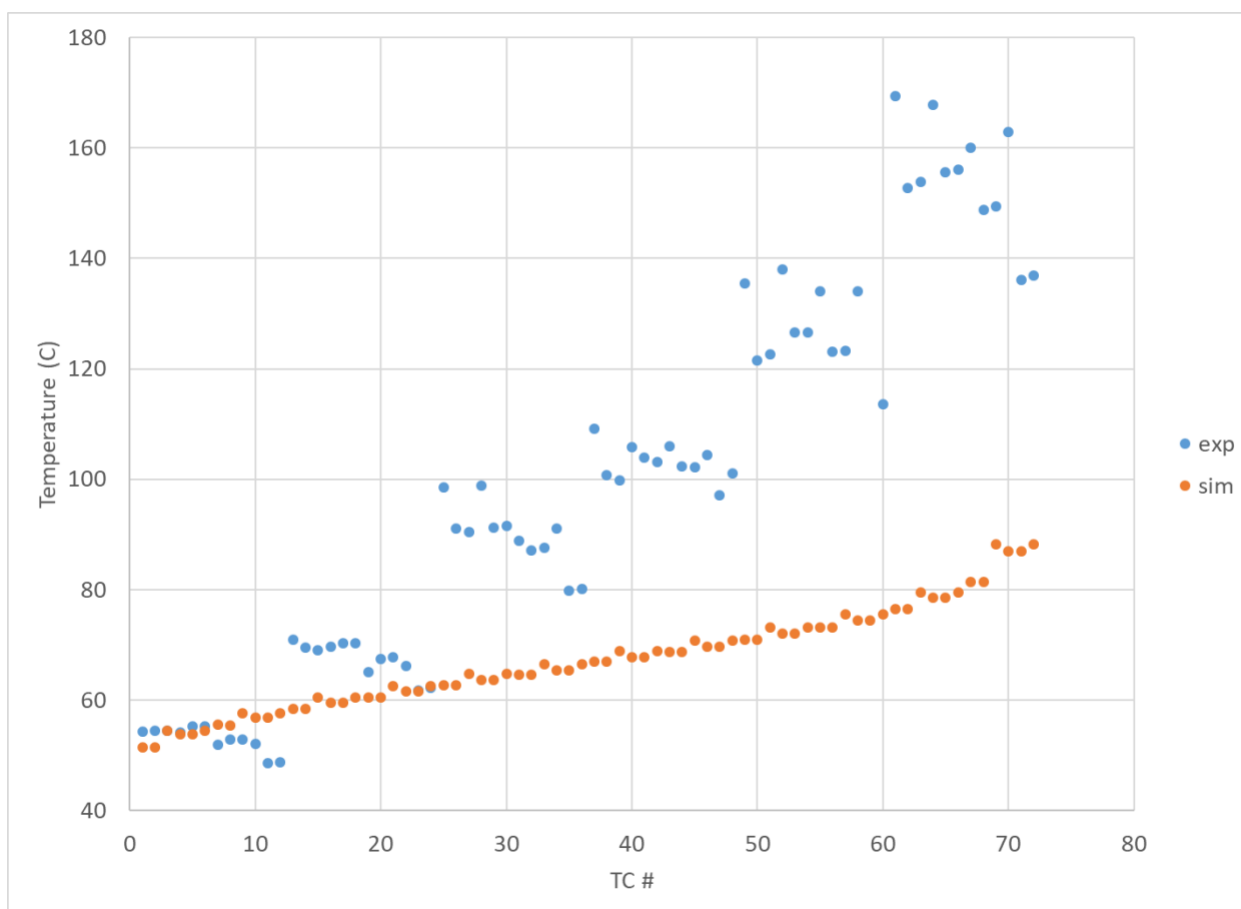


Figure 3-3. Cold wall temperatures for the initial simulations.

Such a large discrepancy in this area seems to indicate either a missing aspect of the physics or a possible improvement in boundary conditions. It was presumed that the physics of

conduction across the cooling panel and insulation is a well-understood phenomenon and that the chance of uncertainty in this aspect being the primary source of error was small. Thus, two main investigations were undertaken to better understand and perhaps explain the reasons for these discrepancies. The first was a testing of the assumption that the side insulation on the cooling panels was solid, i.e., testing whether possible leakage flow between the two sides of the cavity could substantially impact and explain the results. The second was a testing of the adiabatic assumption on the side walls. This was performed by direct addition of physical insulation structures to the model to see if conduction across this outer insulation could provide substantial heat transfer to the cold side. Findings of these two investigations are described below.

3.2.1 Insulation Porosity

The test cases with porous insulation were the same as the base cases, except that the side insulation was changed from a solid region to a porous region. The insulation was still assumed to be opaque, with radiation heat transfer occurring only within each respective side of the cavity; thus, only the impacts of convection heat transfer between the sides are considered. The porous resistance was assumed to be “inertial” in nature, such that the resistance is αV^2 where α represents the loss coefficient and V represents the velocity. Two different porous loss coefficients were tested, namely 10,000 kg/m⁴ and 100,000 kg/m⁴. The coefficients are applied isotropically within the medium. These values are relatively arbitrary high resistance values and simply represent two cases for which the insulation is assumed to still provide substantial flow resistance, just not to the extent assumed previously.

Figure 3-4 and Figure 3-5 provide the predicted temperature distributions on the cold wall as compared to experimental data for the two different cases. It is seen that the inclusion of porosity for the side insulation, even at the very small values tested here, has a large impact on the temperature distribution in the cavity. In fact, the temperature trend for the 100,000 kg/m⁴ resistance coefficient matches the experimental trend very well. Figure 3-6 shows that as compared to the base case, the predicted temperature distributions are similar in features, just primarily with reduced bulk temperature on the hot side of the cavity and correspondingly increased bulk temperature on the colder side. This suggests that potential porosity of the insulation could be a major factor in the temperature distribution within the cavity and should be considered in any studies where it is desirable to know the cavity wall temperatures to higher accuracy. Experimental testing of the insulation may prove useful for obtaining an accurate resistance coefficient.

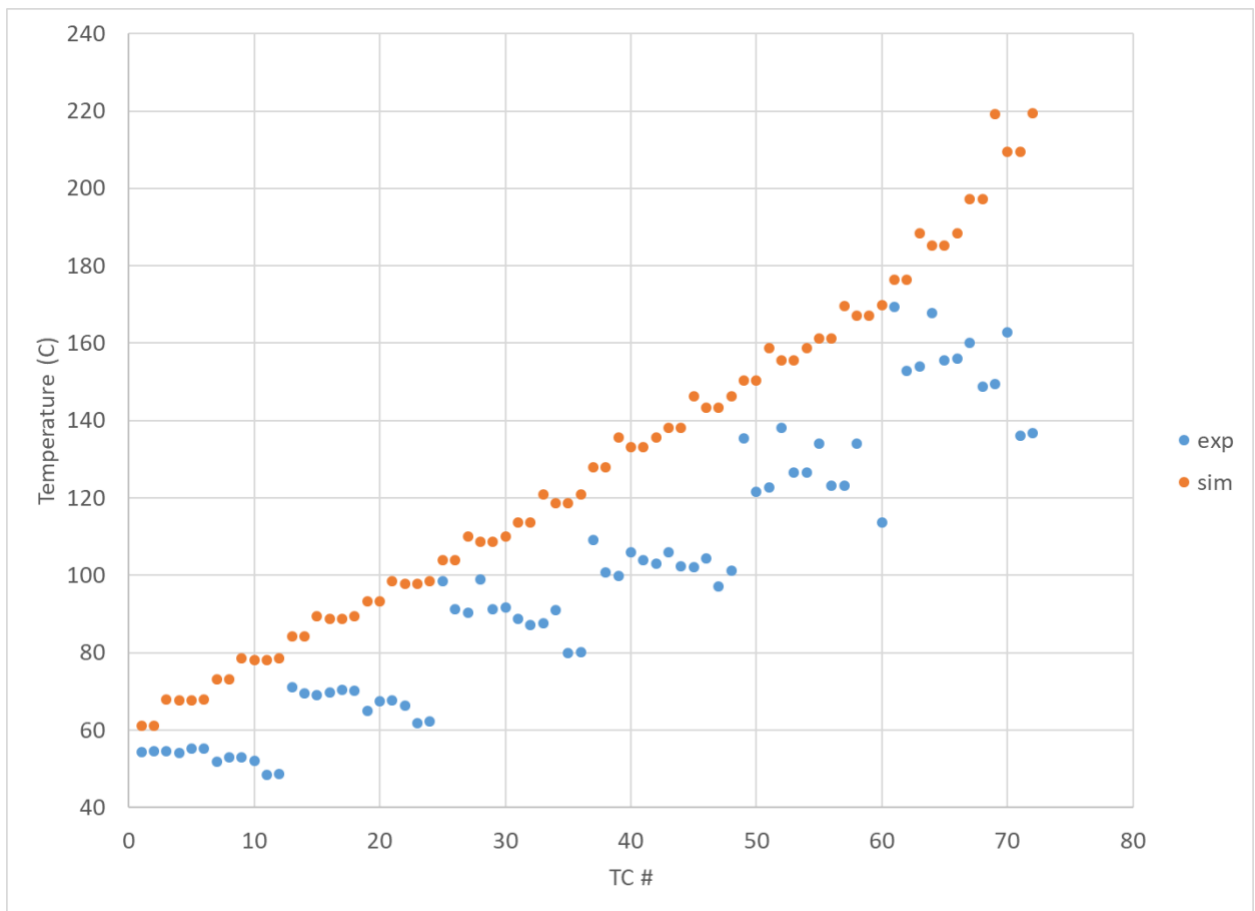


Figure 3-4. Cold wall temperature distribution for the 10,000 resistance case.

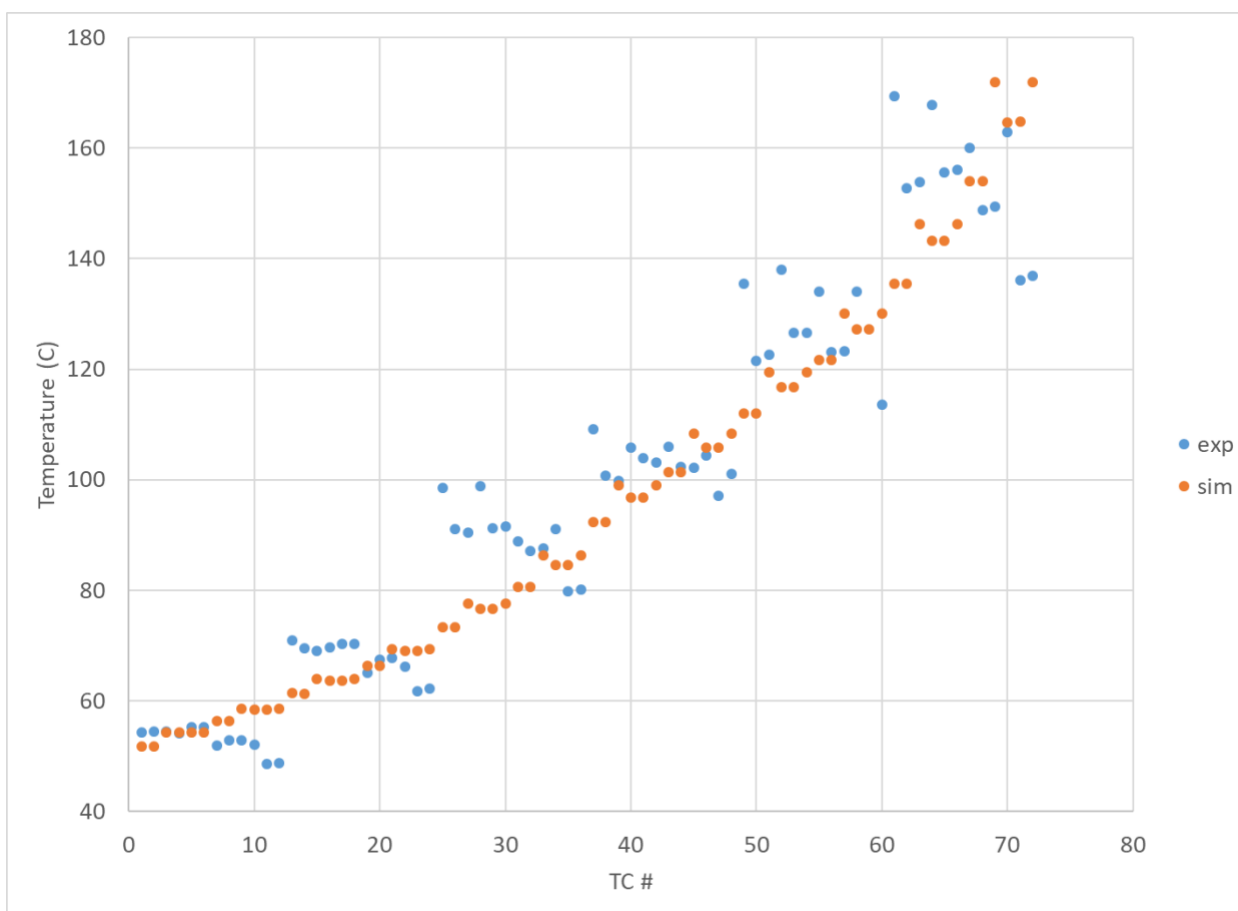


Figure 3-5. Cold wall temperature distribution for the 100,000 resistance case.

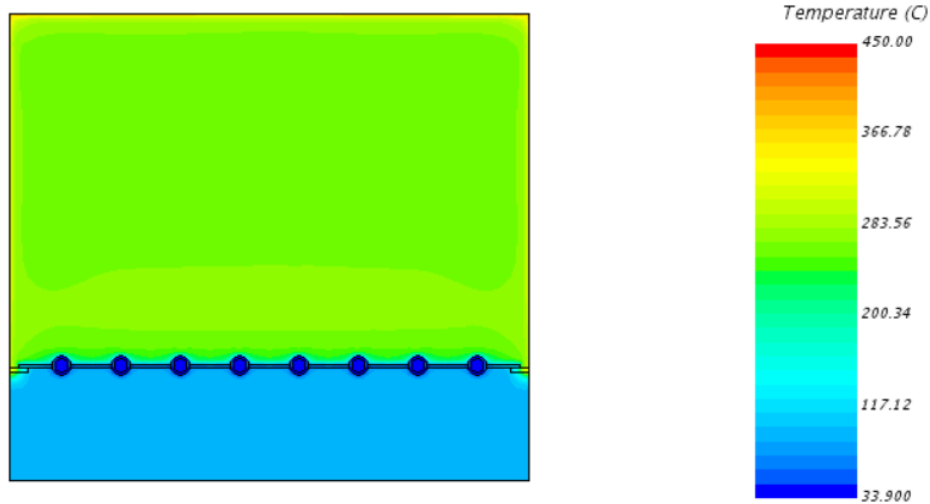


Figure 3-6. Temperature distribution at the cavity midplane for the 100,000 resistance case.

3.2.2 External Insulation Heat Transfer

Another potential avenue for heat transfer to the cold side of the cavity is via the outside insulation surrounding the cavity. To test the impact of this, the external insulation as detailed in the water NSTF design report [3-3] was added to the outside of the cavity. This included a thin layer at the top and bottom of the cavity, which were modeled with adiabatic conditions. The ceramic heaters were added as well, and a uniform volumetric heat generation of the electric power was applied. A constant temperature sink at all the other outer surfaces of the model was applied with a room temperature condition. The thermal conductivities were assumed to be two times higher than the manufacturer-provided values as an attempt to account for the tendency of conductivities to increase with higher temperature. Note that there is significant uncertainty in some of these modeling parameters, and that some areas of the cavity are in actuality non-homogeneous regions with sharp conductivity gradients that are approximated as uniform here for simplicity. But this is a simple proof of principle calculation for which such approximations will suffice.

By comparing Figure 3-7 with Figure 3-2, it is clear that there is substantially more heat transferred to the cold side of the cavity than in the base case, and that the external insulation may not be as perfect as assumed. However, as seen in Figure 3-8, there becomes a stronger lateral gradient in the simulation that is not seen in the experiment. The TC numbering on the cold wall is such that every 3rd TC is closer to the edges, while the preceding two are symmetric and closer to the center. This illustrates that the heat transfer modeling from the insulation may not be realistic, and that it currently appears to induce a “cornering effect” that is not seen in experiment.

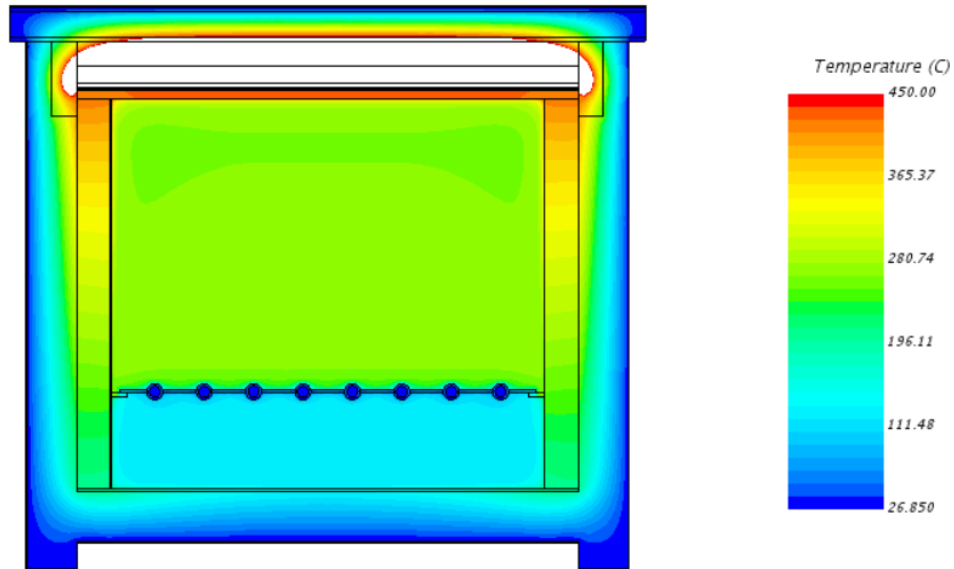


Figure 3-7. Predicted temperature distribution for the case with external insulation modeled. Note that the white region represents a clipping of temperatures above the 450 °C axis limit.

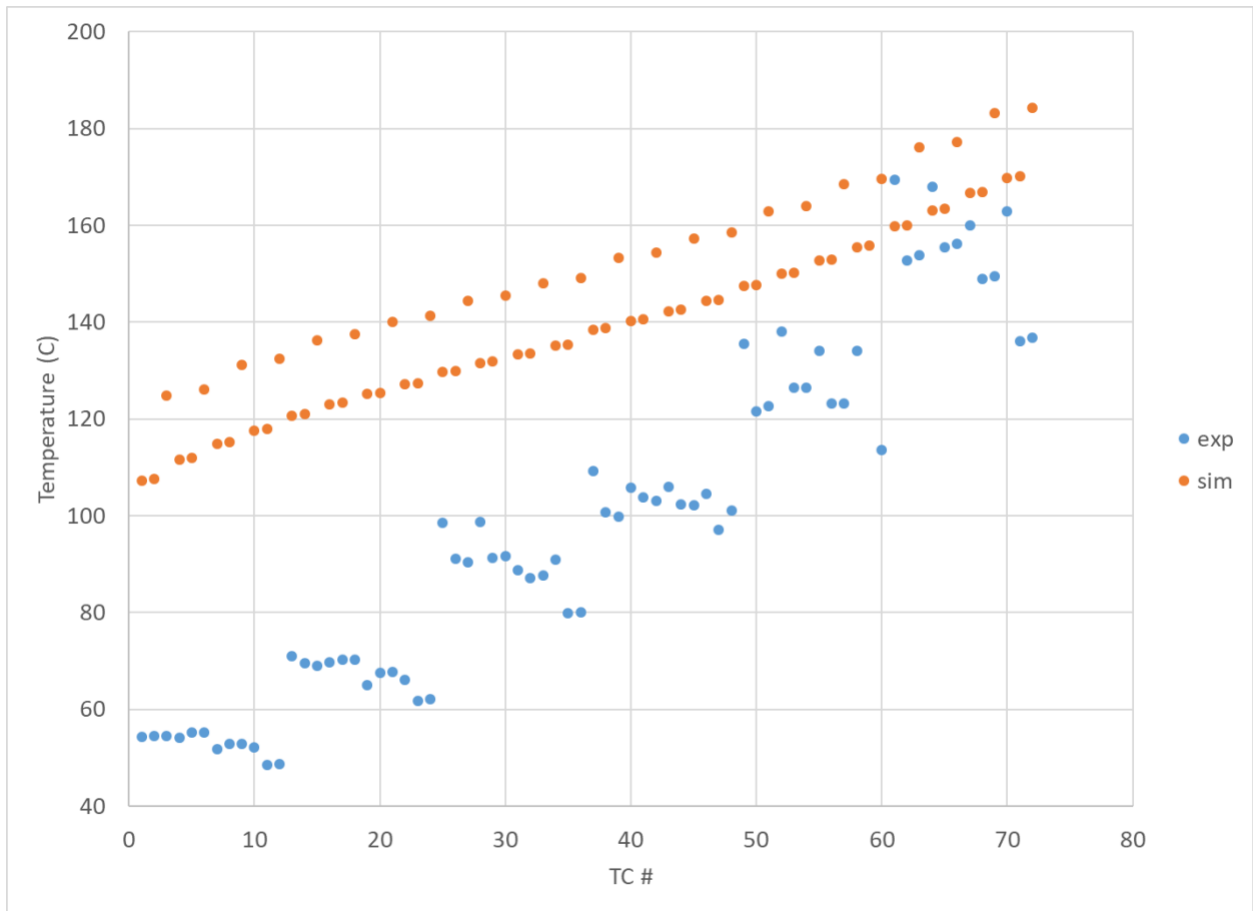


Figure 3-8. Cold wall temperature distribution for the case with external insulation.

The findings from this external insulation case suggest that for the water NSTF, where the cavity is not “open” and there is only indirect heat transfer between the hot and cold sides of the cavity, that perhaps the adiabatic approach is not enough to yield good temperature predictions in the cavity. It also appears that the porous side insulation may be a more straightforward and realistic way of achieving a more representative temperature distribution within the cavity. But it should be noted that the actual impacts of this distribution on the temperature distribution of the water, and hence the macroscopic flow behavior of the primary system, were found to be quite small. Figure 3-9 and Figure 3-10 provide the riser liquid temperatures for the base case and the case with external insulation, respectively. The TC numbers in these cases increase for riser 1 through riser 8 and then proceed to the next elevation, with 6 axial levels in all. Agreement with the experimental data is found to be reasonably good in both cases, but it is also notable that both cases have very similar values despite having very different boundary conditions in the cavity. The specific heat of water is so high, and the temperature rise so small, that the water temperatures are shown to be robust with respect to changes in boundary conditions. This gives some confidence that the nuances of the cavity modeling may have more impact on local temperature conditions in the cavity than on the macroscopic behavior of the system.

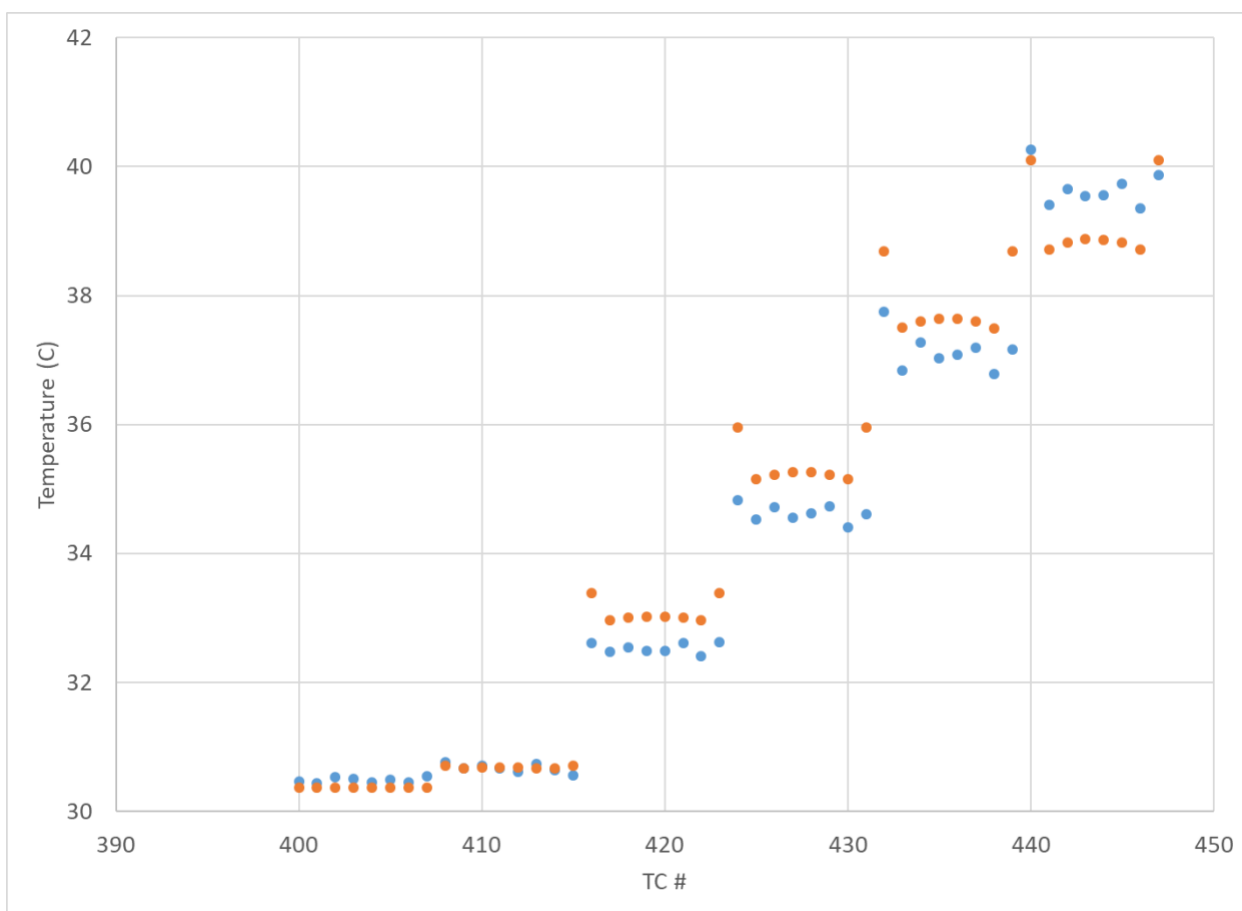


Figure 3-9. Riser liquid temperatures for the base case.

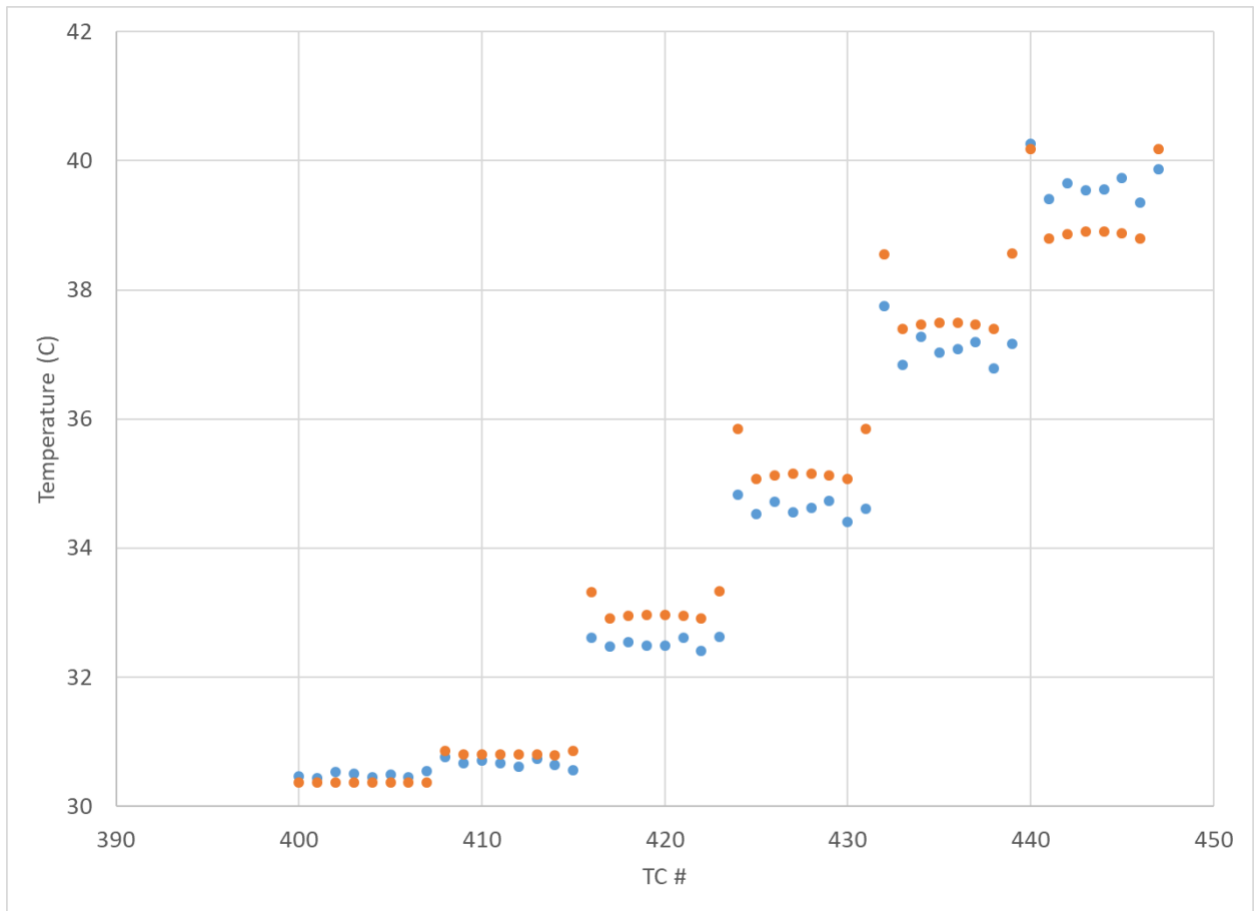


Figure 3-10. Riser liquid temperatures for the case with external insulation.

3.2.3 Impacts of Header Geometry

As mentioned in Section 3.2.1, the work demonstrated above was performed under the assumption that the distribution to each riser tube was “perfect”; i.e., that it was not governed by conditions upstream or downstream of the cavity, but simply by the buoyancy head provided by the heat source from the cavity. In reality, there is an additional form loss that accompanies the flow distribution in the inlet and outlet headers to/from each tube and the bulk flow.

An expanded cavity system was simulated using the geometry in Figure 3-11. This geometry was truncated from the master CAD model described in Section 3.1. Points sufficiently far from the headers to allow for sufficient flow development were chosen as the inlet and outlet of the domain. For simplicity here, the inlet was a forced flow case based on the experimentally measured mass flow rate for Run052. The main goal was to establish any potential nonuniformity of the flow caused by the headers, and its impact on temperatures and flow behavior in the cavity region.

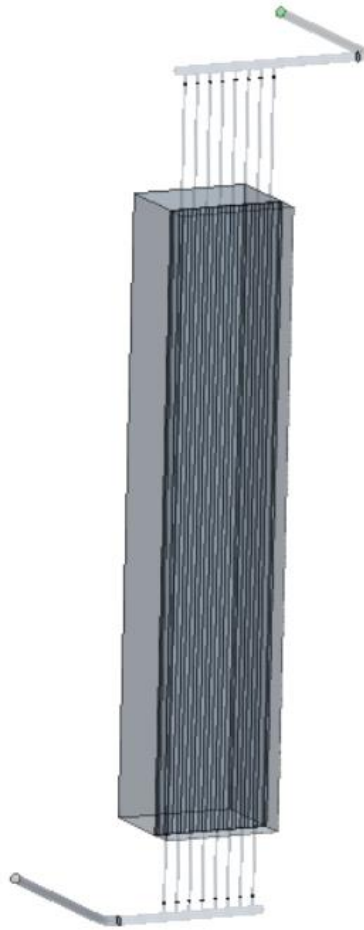


Figure 3-11. Expanded cavity simulation domain including the inlet and outlet headers.

Results for the CFD simulation are provided in Figure 3-12 and Figure 3-13 for the inlet header, and in Figure 3-14 and Figure 3-15 for the outlet header. Note that the headers are of straightforward design, essentially amounting to a rounded cap at the end of the standard piping. The inlet header demonstrates clear non-uniformity of the flow. The 1st riser, i.e. closest to the inlet pipe, features a very strong separation that contributes to a higher pressure drop. The amount of separation at the tube inlet generally decreases from tubes 1 to 8. It appears, as expected, that the flow is largely developed by the entry of the test section.

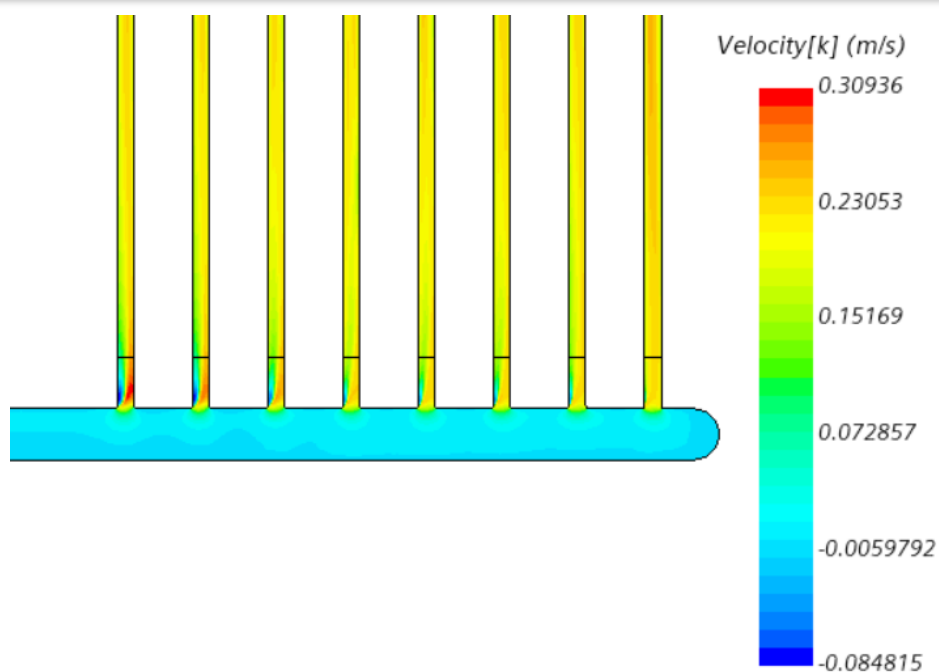


Figure 3-12. Axial velocity at the inlet header midplane.

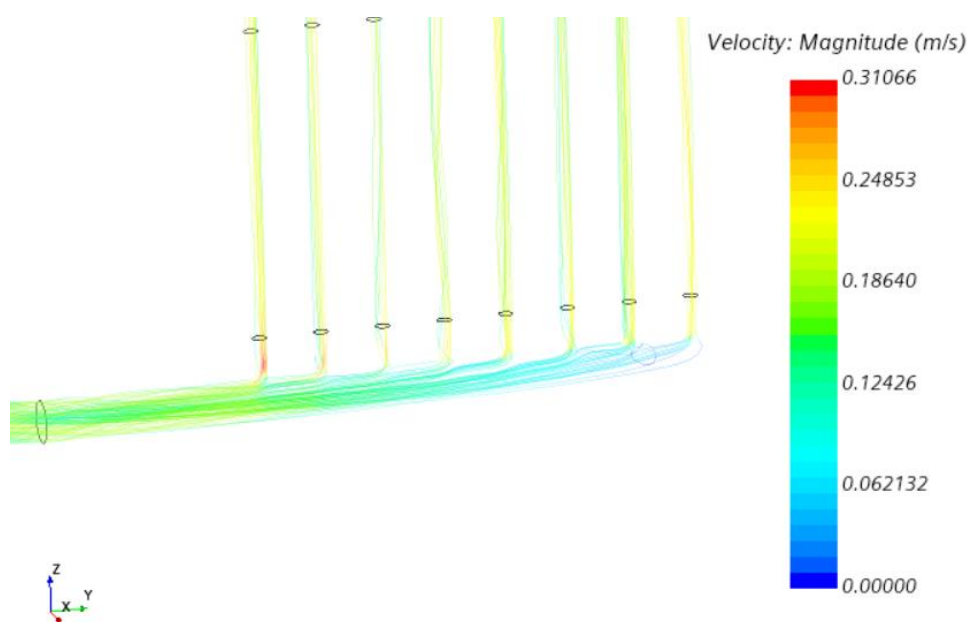


Figure 3-13. Flow streamlines at the inlet header.

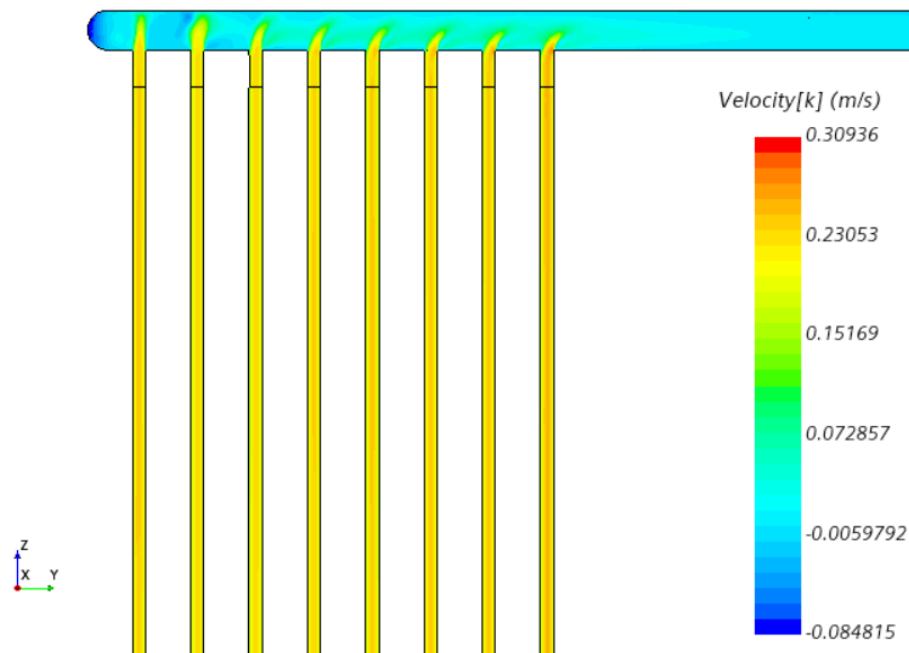


Figure 3-14. Axial velocity at the outlet header midplane.

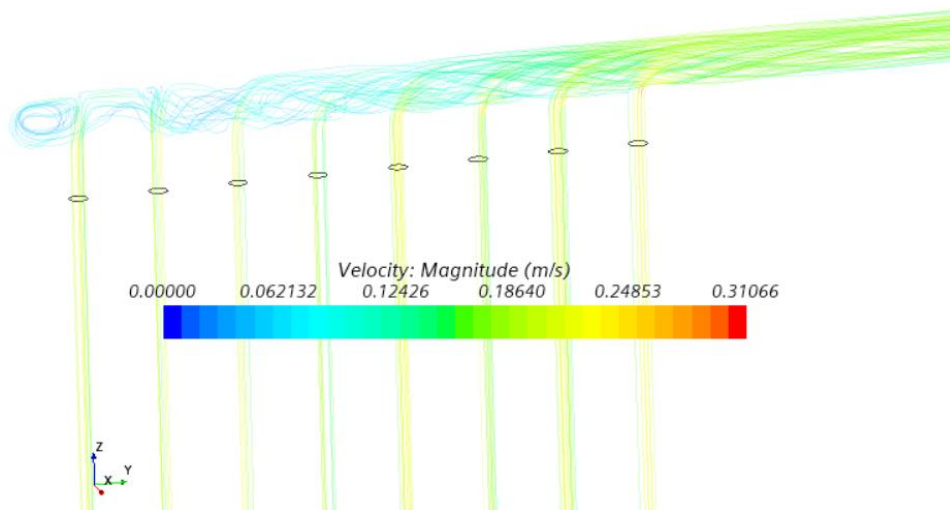


Figure 3-15. Flow streamlines at the outlet header.

The streamlines indicate that in the outlet header there is a recirculation region at the outlet header cap, and potentially some swirling flow. There is a bend not very far downstream (Figure 3-11) that could potentially cause the asymmetry and swirling in the flow. The header flow distributions do indeed demonstrate an influence on the behavior in the cavity. It is noted that the outermost risers/tubes typically see elevated heat transfer due to closer proximity to the side cavity walls. So given the results from the flow distribution, it should be expected that Riser 8 has a lower temperature rise than Riser 1, and that there is a corresponding “tilt” from higher at Riser 1 to lower at Riser 8 for the riser temperatures. This tilt is developed over the axial length, and does not exist at the inlet. This is in fact what is seen in the experimental data, as shown in Figure 3-16. As was previously seen in e.g., Figure 3-10, without the explicit modeling of the

headers, this “tilt” is not seen. Prior to this modeling effort, whether the tilt was physical or instead an instrumental anomaly was uncertain. The explicit modeling of the flow in the headers and cavity provides some evidence that the system and instruments are functioning correctly and that the skewed temperature distribution is indeed physical.

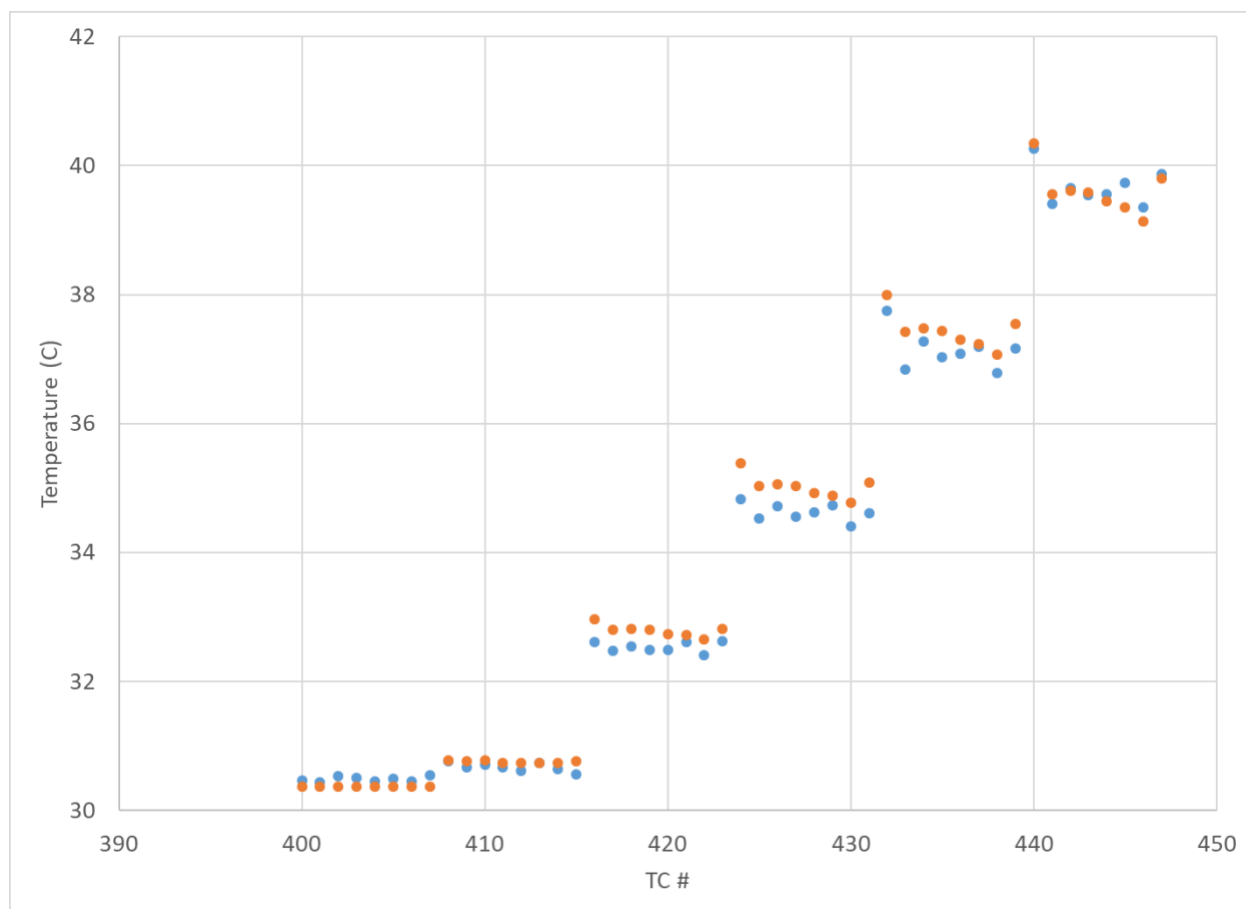


Figure 3-16. Riser liquid temperatures for the case with headers modeled.

3.3 Large Eddy Simulation of a Cavity Unit Cell

As has been shown in the preceding sections, the thermal boundary conditions of the cavity walls are somewhat uncertain and may have localized effects due to the details of the insulation and structural supports. These can impact the flow distributions and peak temperatures in the cavity. The side cavity walls in the NSTF are present essentially due to the practical need to constrain the size of the experiment. In an actual RCCS, these side walls will either not be present or will likely be substantially further apart. A full-scale RCCS will also likely have far more coolant tubes/ducts.

This presents some motivation to perform a so-called “unit cell” study of the cavity. This study could help quantify any potential impacts of the side walls, while also eliminating the issues with uncertainty in the boundary conditions. Such a study has been begun for the water-

cooled NSTF system. Figure 3-17 provides the geometry. Periodic boundary conditions are applied on the lateral sides of the domain, while the standard heat flux is provided at the hot wall and the cold wall is assumed to be adiabatic. The full cavity height is simulated, with adiabatic conditions on the top and bottom of the cavity. The water flow in the tube is simulated as well by an Elliptic Blending Reynolds-Stress Model (EBRSM), and is entirely driven by buoyancy from the heat source from the cavity.

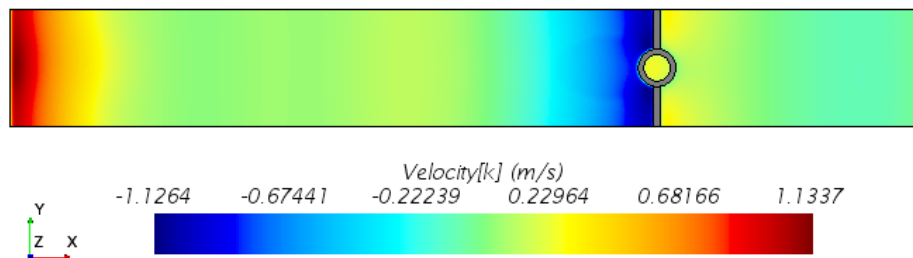


Figure 3-17. Base case axial velocity for the water-cooled NSTF cavity unit cell.

Another benefit of the unit cell case is that it is small enough such that it can be simulated with high-fidelity CFD approaches and used as a validation case for standard RANS models. While these RANS models have been used in prior work on NSTF with some success, the validation case is somewhat lacking. Notably, the NSTF cavity in particular only has temperature measurements. Given the aforementioned uncertainty and difficulty in providing accurate boundary conditions at the walls, using only thermal-based measurements for validation may not provide a rigorous assessment of the lower-fidelity model accuracy. Even so, high-Rayleigh turbulent natural convection heat transfer can present modeling challenges for the typical turbulent heat flux models that are often used in industry and additional validation is always welcome.

For these reasons, a unit cell simulation with Large Eddy Simulation (LES) has been designed and is currently being performed. The WALE model is being employed. The mesh sizing of the case has been constructed in part based on the predicted Taylor length scales provided by a precursor URANS computation. The predicted unsteady velocity from the URANS model, as well as the predicted ratio of the mesh sizing to the Taylor scale, are provided in Figure 3-18 and Figure 3-19, respectively. The sizing has been established and computations are currently ongoing. The LES computations are expected to be completed in FY22, along with comparisons with various URANS and turbulent heat flux modeling approaches.

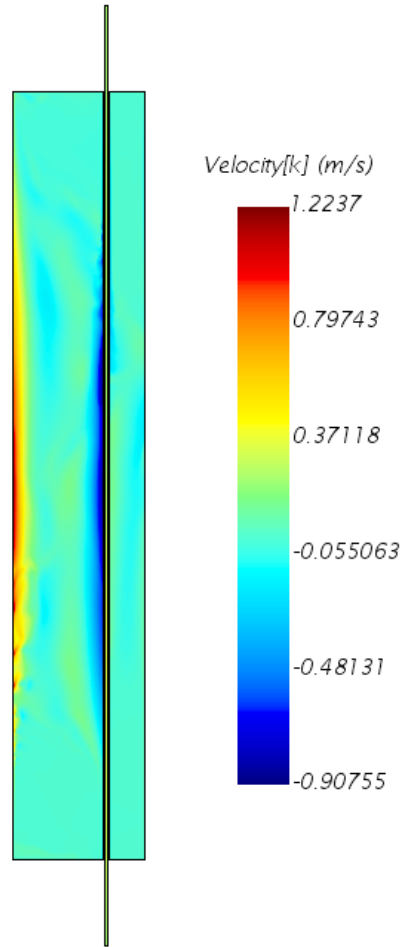


Figure 3-18. Axial view of the URANS unsteady axial velocity for the unit cell study.

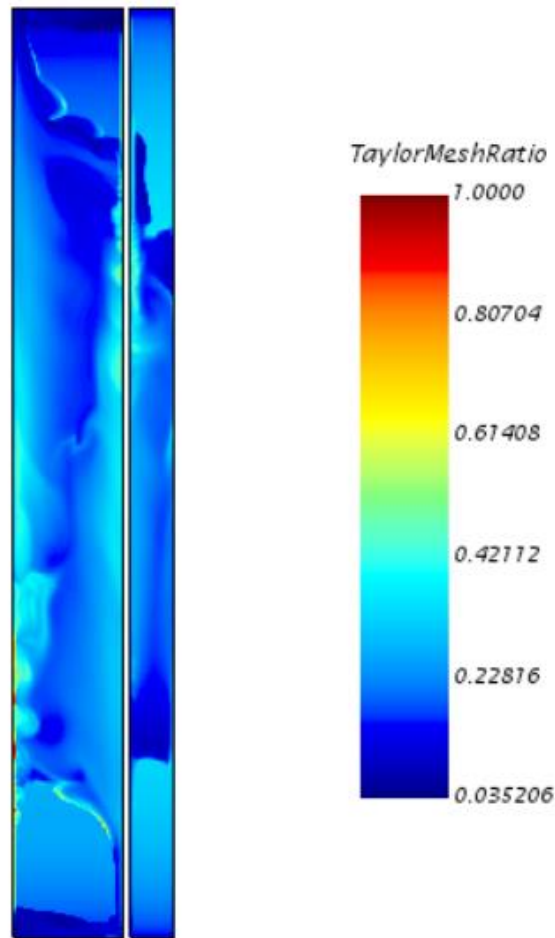


Figure 3-19. Ratio of mesh size to Taylor length scale predicted by URANS.

3.4 Single-phase Full System Simulation

Given the relatively low Reynolds number and velocity in much of the water loop, it could potentially be feasible to investigate small-scale transients (order of hours) using CFD. While the two-phase modeling could cause some complications, it was decided to test the feasibility of the full geometry CFD approach. A CFD model was generated based on the full geometry CAD as established in Section 3.1. Some initial simplifications were made: notably the nominal free surface of the water storage tank was treated as a slip wall. All pipe walls outside of the cavity and tank were treated as adiabatic.

During normal steady NSTF operation, the temperature is controlled by an external chiller loop that takes water from the tank and cools it, then sprays it back into the tank by means of a sparger at the top. This is a complicated process that is not practical to model explicitly in CFD. Thus, for the initial testing of the model, a negative heat flux is applied around the external wall of the tank, such that the heat transfer into the system via the heated wall in the cavity is balanced by the heat transfer out of the system in the storage tank. Different boundary conditions will be tested in the future to pick the one that is most accurate, practical, and numerically stable. A temperature condition at e.g. a portion of the downcomer pipe wall may need to be applied to ensure that the experimentally achieved cooling is matched by the simulation.

The following results are very preliminary and only serve to show that the model is at an early stage of development, but is currently being advanced and tested. The current mesh is very coarse at only roughly 2 million cells, and will need to be refined, particularly in the tank. Figure 3-20 shows the flow at the midplane of the storage tank. As the tank inlet flow is hotter than the bulk tank temperature, the jet rises axially due to buoyancy. The jet interacts with both the far wall and the upper free surface, impinging right near the corner. This is behavior that needs to be investigated further in future work to ensure that certain modeling approaches, e.g. neglecting the cover gas in the tank, are accurate for the case.

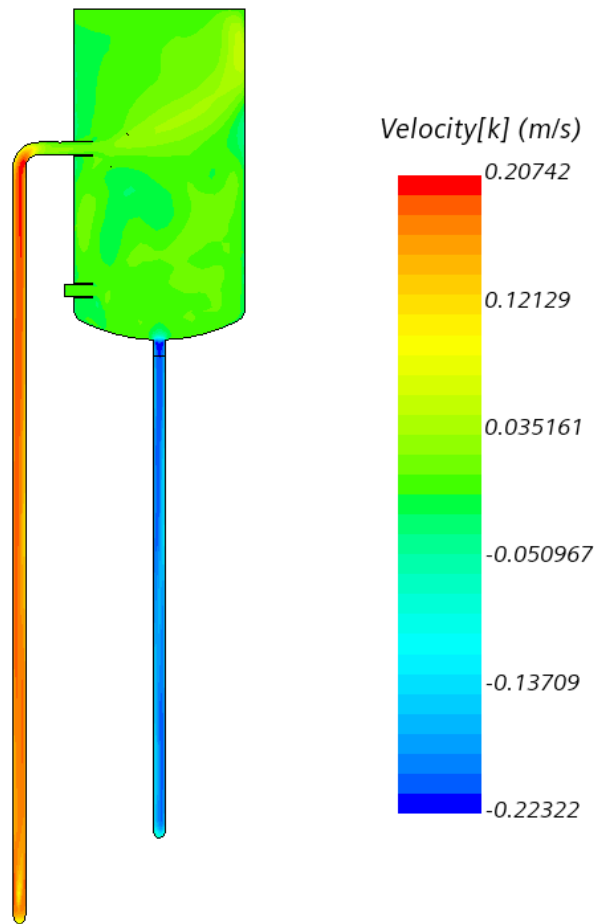


Figure 3-20. Axial velocity patterns in the vicinity of the water storage tank for the full geometry model.

Figure 3-21 provides the velocity vectors for the entire water loop. The “clustered” areas are ones with substantial directional change. It is seen that much of the system features largely one-dimensional flow, with major exceptions being the inlet and outlet headers to the cavity and the storage tank. The other changes are 90° elbows that could in principle be handled with acceptable accuracy by a 1-D system code. This opens up the possibility of performing coupled RELAP5/STAR-CCM+ simulations that could potentially reduce computation time and improve transient predictions.

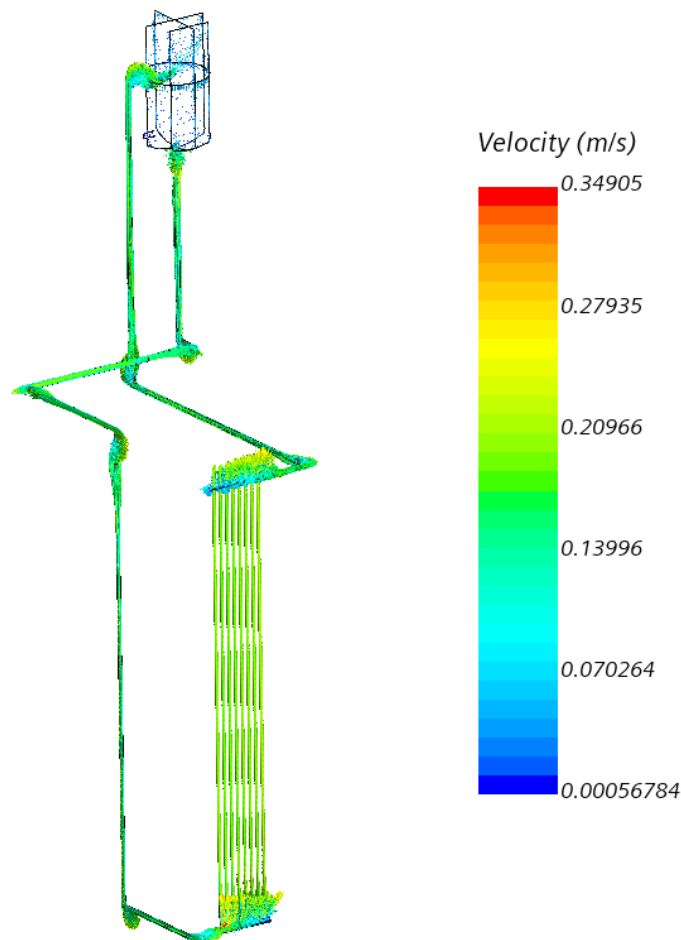


Figure 3-21. Velocity vectors for the full geometry simulation.

3.5 Summary and Future Work

Advancements in CFD modeling of the NSTF were made on numerous fronts in FY21. The first comparisons of the CFD simulations against experimental data were performed. Discrepancies were found in the cavity and addressed by looking deeper into the assumptions of the modeling, notably the methods in which heat can transfer from the hot side to the cold side of the cavity. Experimental evidence, corroborated by CFD, suggested that the edge insulation may be more porous than was previously thought, causing unexpected thermal exchange between the two sides of the cavity. However, this can be partially accounted for in modeling to improve the temperature predictions in the cavity.

Some of the first CFD simulations that delved deeper into the impacts of the NSTF system outside of the cavity were also performed in FY21. The inlet and outlet headers were modeled in detail with CFD, and were found to yield reduced mass flow in Riser 1 and elevated mass flow in Riser 8. These features combine to create an asymmetric temperature profile across the risers. This served as a theoretical basis for some experimental results that were previously uncertain.

Some initial steps were also taken toward expansion of the modeling practices. An LES unit cell computation was designed and initialized. It is hoped that this can provide beneficial validation data in the lack of experimental velocity data in the heated cavity. A preliminary full-geometry NSTF CFD model was also built, and testing was begun. This may lead to the possibility of performing standalone CFD or coupled RELAP5/CFD simulations of transients in the future.

Future work will focus on continued clarification of flow physics in the three-dimensional areas of the NSTF, namely the cavity and the tank. Detailed studies of the tank in particular have yet to be performed, and the mixing and potential stratification in this area can clearly have an impact on the transient behavior. Impacts of the free surface on mixing is a topic of interest in this matter. Another future work is to analyze the LES results and to use them to validate lower-fidelity RANS models. A final area of work is the continued development of the full-geometry NSTF model, which can be used in whole or as part of a coupled simulation to potentially improve predictions of mixing and three-dimensional flow in transient analyses.

References

- [3-1] Lv, Q., Kraus, A., Hu, R., Bucknor, M., Lisowski, D., & Nunez, D. (2017). Progress Report on Computational Analyses of Water-Based NSTF. ANL-ART-103, Argonne National Laboratory.
- [3-2] Star-CCM+ (2020). CD-adapco, LTD. (A Siemens Company).
<https://mdx.plm.automation.siemens.com/star-ccm-plus>.
- [3-3] Lisowski, D., Gerardi, C., Hu, R., Kilsdonk, D., Bremer, N., Lomperski, S., Kraus, A., Bucknor, M., Lv, Q., & Farmer, M. (2017). Water NSTF Design, Instrumentation, and Test Planning. ANL-ART-98, Argonne National Laboratory.

References

Lv, Q., Kraus, A., Hu, R., Bucknor, M., Lisowski, D., & Nunez, D. Progress Report on Computational Analyses of Water-Based NSTF. ANL-ART-103, Argonne National Laboratory, 2017.

D. Lisowski, C. Gerardi, R. Hu, et al., “Water NSTF Design, Instrumentation, and Test Planning,” ANL-ART-98, August 2017.

The RELAP5-3D Code Development Team (2015). RELAP5-3D Code Manual Volume II: User’s Guide and Input Requirements. INL/MIS-15-36723, Idaho National Laboratory.

Filho, F. A. B., Sabundjian, G., Ribeiro, G. H., & Caldeira, A. D. (2017). Assessment of RELAP5 matrix solvers for a two-phase natural circulation loop. *Annals of Nuclear Energy*, 105 (207), pp. 249-258.

Cengel, Y. A., (2002). *Heat Transfer: A Practical Approach*, Second Edition. McGraw-Hill Education.

Star-CCM+ (2020). CD-adapco, LTD. (A Siemens Company).
<https://mdx.plm.automation.siemens.com/star-ccm-plus>.

Acknowledgements

This work is funded by U.S. Department of Energy Office of Nuclear Energy’s Advanced Reactor Technology (ART) program. We gratefully acknowledge use of the Bebop cluster in the Laboratory Computing Resource Center and the Eddy cluster in the Nuclear Science and Engineering Division at Argonne National Laboratory.



Nuclear Science and Engineering Division

Argonne National Laboratory
9700 South Cass Avenue, Bldg. 208
Argonne, IL 60439

www.anl.gov



Argonne National Laboratory is a U.S. Department of Energy
laboratory managed by UChicago Argonne, LLC